International Journal of Hydrogen Energy 72 (2024) 694–715

Contents lists available at ScienceDirect

International Journal of Hydrogen Energy

journal homepage: www.elsevier.com/locate/he

Review of the production of turquoise hydrogen from methane catalytic decomposition: Optimising reactors for Sustainable Hydrogen production

Aryamman Sanyal [a,*], Weeratunge Malalasekera [a], Hemaka Bandulasena [b], K.G.U. Wijayantha [c]

[a] Wolfson School of Mechanical, Electrical and Manufacturing Engineering, Loughborough University, Epinal Way, Loughborough, LE11 3TU, United Kingdom
[b] School of Aeronautical, Automotive, Chemical and Materials Engineering, Loughborough University, Epinal Way, Loughborough, LE11 3TU, United Kingdom
[c] School of Water, Energy and Environment, Cranfield University, College Road, Cranfield, MK43 0AL, United Kingdom

ARTICLE INFO

Keywords:
Steam methane reforming
Catalytic methane decomposition
Fixed-bed reactor
Fluidised-bed reactor
Minimum fluidisation velocity
Bubbling regime

ABSTRACT

Hydrogen is gaining prominence in global efforts to combat greenhouse gas emissions and climate change. While steam methane reforming remains the predominant method of hydrogen production, alternative approaches such as water electrolysis and methane cracking are gaining attention. The bridging technology – methane cracking – has piqued scientific interest with its lower energy requirement (74.8 kJ/mol compared to steam methane reforming 206.278 kJ/mol) and valuable by-product of filamentous carbon. Nevertheless, challenges, including coke formation and catalyst deactivation, persist. This review focuses on two main reactor types for catalytic methane decomposition – fixed-bed and fluidised bed. Fixed-bed reactors excel in experimental studies due to their operational simplicity and catalyst characterisation capabilities. In contrast, fluidised-bed reactors are more suited for industrial applications, where efforts are focused on optimising the temperature, gas flow rate, and particle characterisation. Furthermore, investigations into various fluidised bed regimes aim to identify the most suitable for potential industrial deployment, providing insights into the sustainable future of hydrogen production. While the bubbling regime shows promise for upscaling fluidised bed reactors, experimental studies on turbulent fluidised-bed reactors, especially in achieving high hydrogen yield from methane cracking, are limited, highlighting the technology's current status not yet reaching commercialisation.

1. Introduction

Excessive levels of anthropogenic CO_2 emissions in the atmosphere make it the most conspicuous greenhouse gas (GHG) among the rising concern for climate change. CO_2 emissions have been rising as a direct result of increased human activity since the industrial revolution, and it is regarded as more damaging than other GHGs due to its millennia-long lifespan [1]. Countries maintaining their energy security through economic growth and improved living standards have increased energy demand, hence heavy reliance on fossil fuel sources [2,3]. Therefore, mitigation solutions must be implemented to ensure that the emission of CO_2 is controlled and limited.

Carbon budgeting can help set long-term temperature objectives by requiring governments and industries to adopt interim and final mitigation plans to guarantee that renewable energy sources are applied across the global economy [4]. The International Energy Agency (IEA) and the Committee on Climate Change (CCC) have deemed it crucial that hydrogen technologies be implemented in several industrial sectors for an economy to attain net-zero emissions by 2050 [5]. Furthermore, predictions of successful hydrogen technology integration could lower global GHG emissions by 80% compared to 1990 levels [6]. Currently, within the UK economy, special attention has been received, with a hydrogen strategy already being launched aiming to become a "global leader in hydrogen" by 2030 [7].

The hydrogen economy is a potential solution for decarbonising challenging sectors such as the power, transport, and electricity sectors. Hydrogen is a flexible and versatile energy carrier that is regarded as the cleanest fuel with a by-product of water when combusted [8]. Moreover, in terms of mass, hydrogen provides three times more energy (39.4 kWh kg^{-1}) than conventional fossil fuels such as gasoline producing only 13.1 kWh kg^{-1} [8]. Presently, it is evident that both renewable and non-renewable technologies can be used to synthesise hydrogen; and according to Fig. 1, fossil fuels such as coal gasification (18%), oil-based (30%), and natural gas steam reforming (48%) accounts for 96% of total hydrogen production [5,8]. At the moment, fossil-fuel-based production

* Corresponding author.
E-mail addresses: a.sanyal@lboro.ac.uk (A. Sanyal), w.malalasekera@lboro.ac.uk (W. Malalasekera), h.c.h.bandulasena@lboro.ac.uk (H. Bandulasena), upul.wijayantha@cranfield.ac.uk (K.G.U. Wijayantha).

https://doi.org/10.1016/j.ijhydene.2024.05.397
Received 2 February 2024; Received in revised form 7 May 2024; Accepted 26 May 2024
Available online 31 May 2024
0360-3199/© 2024 The Authors. Published by Elsevier Ltd on behalf of Hydrogen Energy Publications LLC. This is an open access article under the CC BY license (http://creativecommons.org/licenses/by/4.0/).

List of abbreviations including units and nomenclature

GHG	Greenhouse gas
UNFCCC	United Nations Framework Convention on Climatic Change
IPCC	Inter-governmental Panel on Climate Change
IEA	International Energy Agency
CCC	Committee on Climate Change
SMR	Steam methane reforming
WGS	Water gas shift
PSA	Pressure swing absorption
CMD	Catalytic methane decomposition
HES	High-energy Sites
VLS	Vapour-liquid-solid
RDS	Rate-determining step
CFD	Computational fluid dynamics
PMM	Porous medium model
PRCFD	Particle-resolved CFD
SEM	Scanning Electron Microscope
GC	Gas Chromatography
XPS	X-ray Photoelectron Spectroscopy
TEM	Transmission Electron Microscopy
AC	Activated Carbon
CB	Carbon Black
XRD	X-ray Diffraction Analysis
BET	Brunauer-Emmett-Teller
TGA	Thermogravimetric Analysis
U_{mf}	Minimum fluidisation velocity
U_{mf}	Minimum bubbling velocity
CNT	Carbon nanotubes

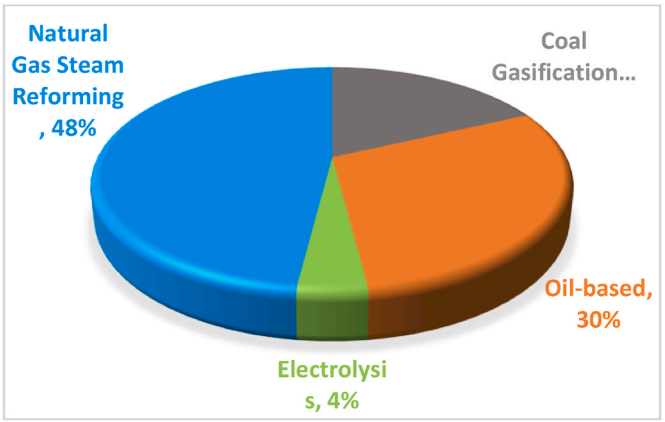

Fig. 1. Hydrogen production using both renewable and non-renewable technologies. Data Source 5,8.

is dominating renewable options due to their high availability, cost-effectiveness, and better efficiency. For instance, hydrogen production using fossil fuel costs $1 per kilogramme (kg) versus $6 per kg from offshore wind energy (data from 2020) [9]. Hence, it may be assumed that growing hydrogen consumption will directly increase GHG emissions, jeopardising the net-zero emission goal.

From Fig. 1, steam methane reforming (SMR) dominates the global hydrogen industry. High demand is allocated within this industry due to SMR bringing a mature process with an efficiency of 76% when manufacturing pure, industrial-grade hydrogen [10]. The natural gas reagent, primarily composed of methane, followed by ethane, propane, and ethylene, alongside nitrogen, CO_2, and H_2S, depending on its source, is preheated to temperatures ranging between 450 and 500 °C before being directed through the reformer tube containing a Ni-based catalyst. [11,12].

Reforming Reaction 1- $CH_4 + H_2O \rightleftharpoons CO + 3H_2$ $\Delta H_{rx} = 206.28$ kJ/mol (1)

Reforming Reaction 2- $CH_4 + H_2O \rightleftharpoons CO_2 + 4H_2$ $\Delta H_{rx} = 164.00$ kJ/mol (2)

Water-Gas shift reaction- $CO + H_2O \rightleftharpoons CO_2 + H_2$ $\Delta H_{rx} = -41.16$ kJ/mol (3)

Both reactions (1) and (2) signify non-identical endothermic reaction pathways, in which they present the synthesis procedure of hydrogen-rich syngas from CH_4 and steam but result in distinct CO and CO_2 by-products [13,14]. Furthermore, almost 12% of the total CO by-product obtained from the reaction mixture in the reformer can undergo the water gas shift (WGS) reaction indicated in step (3) [15]. The WGS allows the CO content to decrease while simultaneously maximising the hydrogen yield [16]. Finally, because SMR generates high impurities in the reformer, a pressure swing absorption (PSA) unit is used to provide a high-purity H_2 stream [16]. A schematic diagram of the reaction process is shown in Fig. 2 [5,11,13–16].

Furthermore, due to research and infrastructure constraints, the production of green hydrogen utilising renewable technologies is still in its early stages. As a result, implementing bridging technology becomes more suitable to tackle current climate variation while renewable technologies continue to advance simultaneously. One such bridging technology is methane cracking. This process bridges the gap between the existing carbon-intensive fossil-fuel-based energy systems and a low-carbon energy economy [17]. Methane cracking involves the production of turquoise hydrogen governed by an endothermic chemical reaction of CH_4, resulting in molecular separation under high temperature, low pressure, and no presence of oxygen [18]. Consequently, elemental carbon particles and hydrogen are generated, as shown in reaction (4).

The reaction scheme for methane cracking involves:

$$CH_4 \rightleftharpoons C_{(s)} + 2H_2 \quad \Delta H^{\circ}_{25\ ^{\circ}C} = 74.8 \text{ kJ / mol} \tag{4}$$

Methane is highly stable due to its symmetrical molecular structure and strong C–H bonds, requiring a significant dissociation energy of 439.3 kJ/mol to break individual C–H bonds. Thus, a high operating temperature is essential [19–21]. To enhance hydrogen yield and lower the temperature (1000-1200 °C) required for the reaction, catalytic methane decomposition (CMD) has been developed over the years using various metal and non-metal catalysts. Transition metals such as nickel (Ni), iron (Fe), and cobalt (Co) have been extensively studied as the primary components for methane cracking. They offer beneficial characteristics such as high permeability for carbon diffusion and produce valuable carbon nanotubes as by-products [21,22]. According to various literature, the following pattern has been established in terms of catalytic activity: Ni > Co > Fe [21,23–25]. Catalysts enhance methane cracking at a moderate temperature by lowering activation energy by accepting electrons from the C–H single bond via partially filled 3d orbitals [19,21]. The metal electronic state and the dispersion of the active sites are the two key characteristics that determine a catalyst's efficiency [23].

Since CMD operates without oxygen, no greenhouse gas (GHG) emissions such as CO_2 and CO are generated. Instead, the generated elemental carbon particles are economically valuable and can incentivise several industries [19]. Carbon particles in the form of "carbon black, CNTs, graphite and graphene" have beneficial characteristics and economic value for commercial applications; hence, this would lower

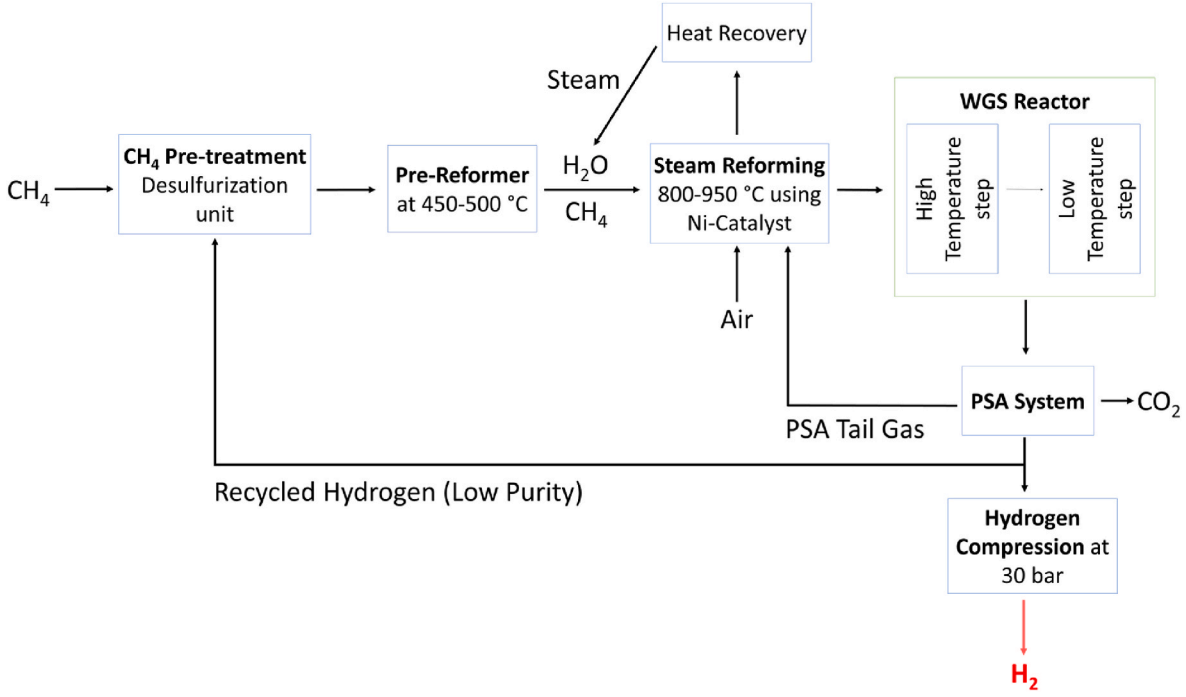

Fig. 2. A schematic diagram signifying the step-by-step process of an SMR reactor that has been evaluated above.

the overall cost of hydrogen generation [26]. Nevertheless, the cost of hydrogen depends on the crystallinity and morphology of the carbon obtained, which varies depending on the reaction conditions [23]. One major drawback of CMD is the potential for coke formation, whereby encapsulated filamentous carbon deactivates the catalyst, raising operational costs due to replacements [19].

Furthermore, SMR would have an energy requirement of 206.28 kJ/mol, although methane cracking requires a lower 74.8 kJ/mol of energy input to synthesise hydrogen [19]. Compared to renewable methods like water electrolysis (286 kJ/mol), methane cracking is still the thermodynamically more advantageous choice [22]. However, CMD has a considerably lower conversion efficiency of 58%, in contrast to SMR, which has 76%. Yet, it is worth noting that the remaining 42% efficiency after CMD results in filamentous carbon particles that can be kept and commercialised. Conversely, in SMR, the remaining 40% is lost as long-lived GHG, resulting in environmental hazard and energy loss [25]. Therefore, CMD appears to be a better alternative after addressing the disadvantages of SMR and renewable technologies.

This review article attempts to conduct an in-depth analysis of the fundamentals of CMD. As there is already a vast knowledge gap with the development of different methane decomposition reactors, the objective of this review paper is to essentially: (a) investigate the principles of reaction mechanisms behind CMD; (b) outline the experimental advantages of fixed-bed reactors in facilitating characterisation techniques and identifying the various instruments necessary for optimising and comparing different catalyst types; (c) interpret the dependent conditions necessary for optimising fluidised-bed reactors; and (d) identify the ideal fluidisation regime for scaling up CMD to an industrial platform.

2. Methane cracking mechanisms

There is still a debate about the mechanism of methane cracking. Different mechanisms have been proposed over the years, but the kinetic parameters (pre-exponential factor, activation energy, and reaction order) of each intermediate elementary reaction step are uncertain [8,22]. Two main models have emerged as prominent in several experimental reports: the free-radical scheme and the vapour-liquid-solid (VLS) model.

2.1. Free-radical scheme

It is well-established that methane molecules are primarily adsorbed on a metal catalyst during methane decomposition. However, various studies have revealed that the surface dehydrogenation reactions, which reduce methyl radicals to their elemental state, can be divided into two mechanism types – dissociative [27–31] and non-dissociative models [32–35]. This distinction is based on the initial C–H bond cleavage time [19,22,36]. The following section will aim to dive deeper into these two hypotheses and determine the rate-limiting steps associated with each mechanism.

Non-dissociative Mechanism: This kinetic model was first approached by Grabke [37], where adsorbed methane molecule initially undergoes surface reaction without cleaving the C–H bonds [19,22]. As depicted in Equations 5–11, the methyl group undergoes a sequence of dehydrogenation processes once methane has been adsorbed on the catalyst surface, leading to hydrogen production [38].

$$CH_4 + S_{(Vacant\ site)} \leftrightarrow CH_4S_{(ad)} \quad (5)$$

$$CH_4S_{(ad)} + S \leftrightarrow CH_3S_{(ad)} + HS_{(ad)}\ RDS \quad (6)$$

$$CH_3S_{(ad)} + S \leftrightarrow CH_2S_{(ad)} + HS_{(ad)} \quad (7)$$

$$CH_2S_{(ad)} + S \leftrightarrow CHS_{(ad)} + HS_{(ad)} \quad (8)$$

$$CHS_{(ad)} + S \leftrightarrow CS_{(ad)} + HS_{(ad)} \quad (9)$$

$$2HS_{(ad)} \leftrightarrow H_2 + 2S \quad (10)$$

$$CS_{(ad)} \leftrightarrow C_{(Ni,\ f)} + S \quad (11)$$

Dissociative Mechanism: As represented in Equation 12–17, this model complements the mechanism stated earlier. However, the primary distinction lies in the initial step, where adsorbed methane molecules undergo chemisorption on the catalyst surface while simultaneously cleaving the C–H bond [38].

$$CH_4 + 2S_{(Vacant\ site)} = CH_3S_{(ad)} + HS_{(ad)}\ RDS \quad (12)$$

$$CH_3S_{(ad)} + S{=}CH_2S_{(ad)} + HS_{(ad)} \quad (13)$$

$$CH_2S_{(ad)} + S{=}CHS_{(ad)} + HS_{(ad)} \quad (14)$$

$$CHS_{(ad)} + S{=}CS_{(ad)} + HS_{(ad)} \quad (15)$$

$$CS_{(ad)} = C_{(dissolved)} + S \quad (16)$$

$$2HS_{(ad)} = H_2 + 2S \quad (17)$$

RDS: Rate-determining Step; S: Vacant Sites; CH_4: Methane; C: Carbon; H: Hydrogen

As distinguished, the rate-determining step (RDS) is represented by Equations (6) and (12), which vary according to the specific mechanism steps. In a reaction mechanism, the RDS is typically associated with the activation of methane molecules. This step is usually the slowest in the reaction mechanism, and it determines the overall rate at which the methane is converted into elemental carbon and hydrogen [22]. However, it is essential to note that the mechanisms discussed above do not account for the formation of filamentous and encapsulation of carbon on the catalyst. Therefore, section 2.2 will provide and in-depth exploration of the vapour-liquid-solid (VLS) model that validates the carbon formation and encapsulation processes.

2.2. VLS model

The formation and growth of carbon nanofibers from a carbon-containing precursor over solid catalysts were explained by Baker et al. in 1972 [39] using a second potential mechanism, the so-called VLS model. This mechanism validates the growth of filamentous carbon on the metal catalyst during methane cracking [39].

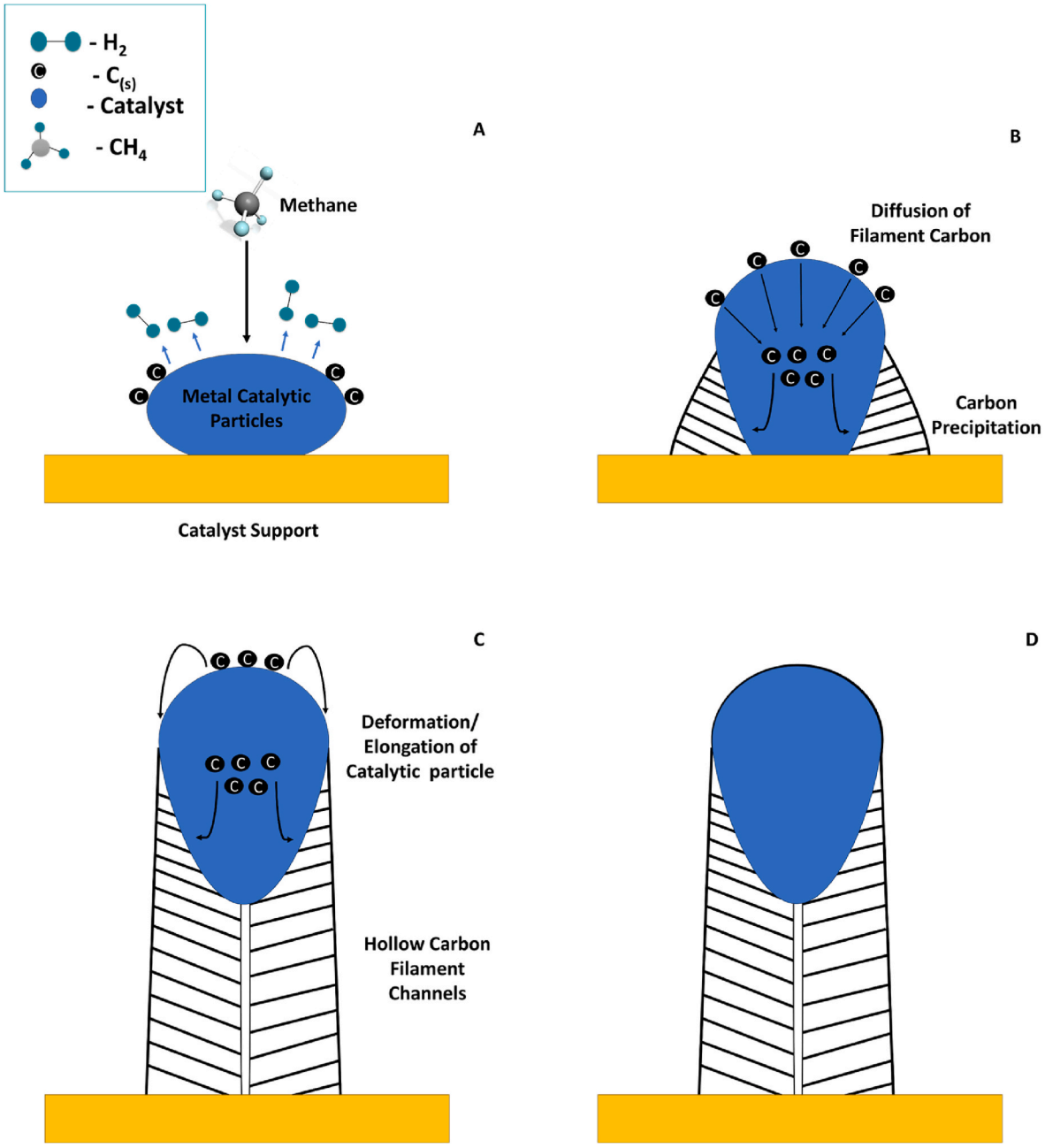

Fig. 3. Demonstrates the step-by-step process of the VLS model. (A) depicts the adsorption of methane on the catalyst surface; (B) reflects the deposition of carbon after the decomposition reaction, followed by its diffusion through the metal particles; (C) and (D) represent the nucleation process, causing deformation of the catalyst particles. (For a more precise understanding, please refer to the key in the top left corner, which highlights the components represented in the figure).

Fig. 3A displays methane gas being adsorbed onto the catalyst surface, undergoing a decomposition reaction, producing elemental carbon and hydrogen. In Fig. 3B, excess carbon deposited on the catalyst surface diffuses through the metal particles, resulting in carbon precipitation on the backside of the catalyst particle at the 'metal-support contact'. The collected solid or hollow carbon filament deposit would push the metal particles away from the support, as shown in Fig. 3C, and eventually, filamentous carbon nucleation commences [19,22].

Nucleation marks the initial stage of filament growth, where the metal-based catalyst possesses liquid-like characteristics and undergoes deformation and elongation (shown in Fig. 3C and D). This phenomenon, occurring at high temperatures, leads to a nucleation rate surpassing the diffusion rate [19]. Here, the metal particle detaches from its support, and hollow channels emerge, inhibiting further precipitation [19,22]. Ultimately, increasing the rate of methane decomposition would exponentially expand the carbon filament growth, resulting in indefinite carbon encapsulation and a complete detachment between the metal catalyst particle and support. As a result, the decomposition rate would slow down due to the deactivation of the catalyst [19]. Therefore, filamentous carbon diffusion through the metal particle is recognised as the RDS [22]. Scanning electron microscope (SEM) images generated by Wei et al. [40] (Fig. 5) clearly illustrate catalyst deactivation from carbon deposition by showing images of both fresh (Fig. 5a,(b),(c),(d)) and spent (Fig. 5A,(B),(C),(D)) catalyst during the methane decomposition process. Furthermore, Konieczny et al. [41] alternatively operated a transmission electron microscopy (TEM) to explore ultrastructure and particle size distribution, offering higher-resolution images of the atomic arrangement within materials [42].

Overall, the RDS from this mechanism is not accounted for within the radical mechanism; therefore, there is still no clarity when determining the RDS. It remains unclear whether the overall RDS involves breaking methane into a methyl radical or the diffusion of carbon into the bulk catalyst [39]. Identifying the necessary mechanism and RDS is crucial before conducting experimental or modelling studies. By interpreting

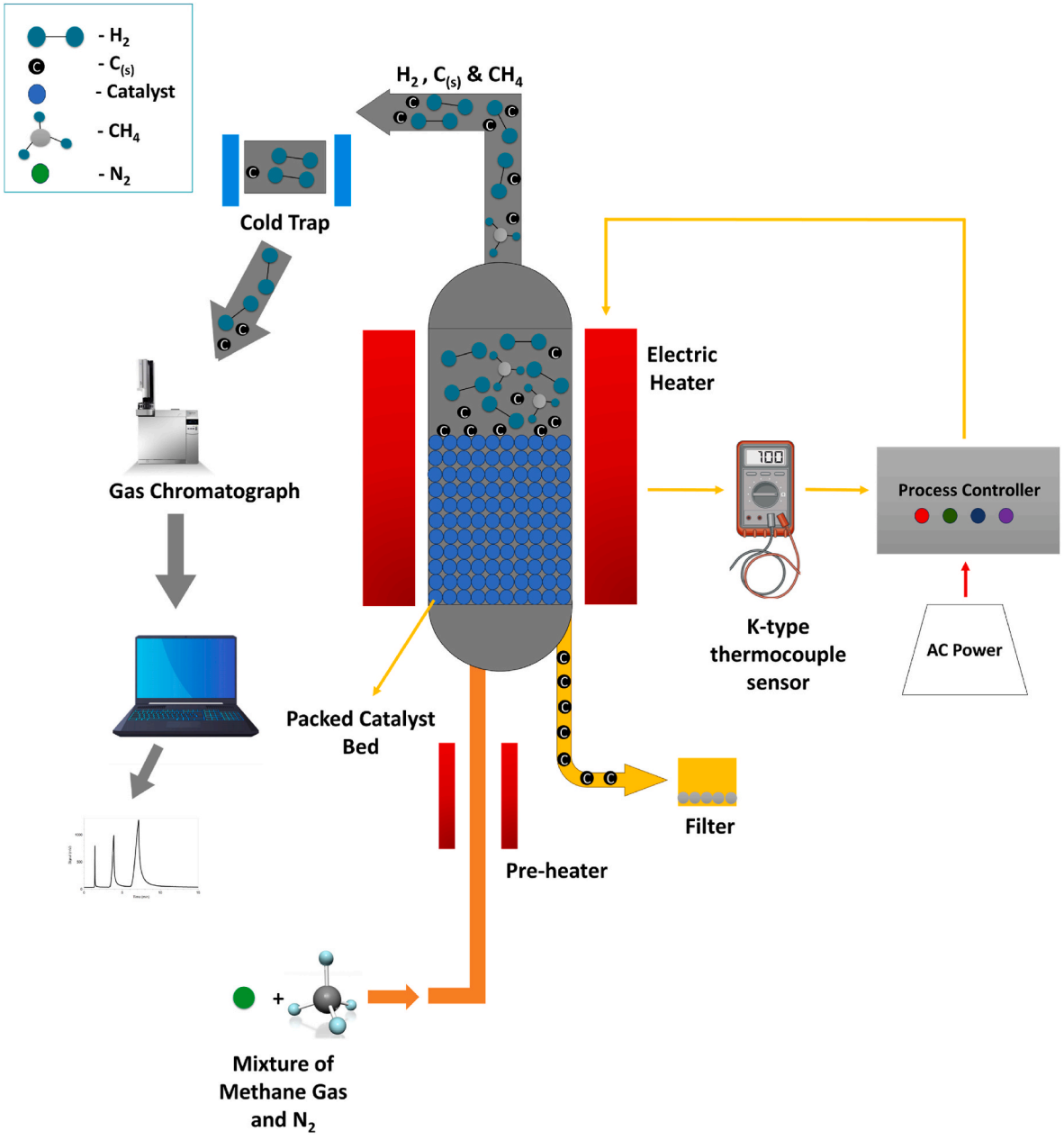

Fig. 4. An experimental set-up that utilises a fixed-bed reactor to conduct catalytic methane decomposition reaction. (For a more precise understanding, please refer to the key in the top left corner, which highlights the components represented in the figure).

the mechanism, researchers can predict the reactor performance and optimise it by adjusting conditions such as temperature, methane flow rate, pressure, and catalyst selection. The following section will delve into the fixed-bed reactor, a standard configuration used for experimental studies in CMD.

3. Fixed-bed reactors

A typical fixed-bed reactor configuration (Fig. 4) starts with catalyst preparation and placement within a quartz tube. Before preheating the furnace, the maintenance of lower-than-atmospheric pressure in the reactor is achieved by introducing inert gases of N_2 or Ar, which lowers the partial pressure of methane, while the overall pressure of the reactor would remain constant at 1 atm [41]. Subsequently, the quartz tube reactor is positioned in a high-performance furnace and heated to its desired temperature, determined by the catalyst and parameter of the reactor. Methane is simultaneously injected from its storage tank through the bottom of the reactor [43,44]. The reactor's catalyst bed temperatures are experimentally controlled and monitored by using a K-type thermocouple sensor, and a mass flow meter controls the methane feed rate [43]. Consequently, thermal decomposition is optimised with careful management of the methane flow rate, resulting in increased production of hydrogen and solid carbon. Analysis of the final product is examined using a gas chromatograph coupled to the reactor's output, as depicted in Fig. 4. Here, a time-dependent study on the catalytic activity can be examined by observing the hydrogen yield and methane conversion at distinct time intervals [43]. Currently, a lot of experimental research on CMD uses a fixed-bed reactor. The specific aims and methodology may differ depending on the study goals (see Appendix 1); however, the use of fixed-bed reactors allows for research on the reaction kinetics, catalyst performance, and process optimisation in methane cracking.

Additionally, the simulation of a fixed/packed-bed reactor using multiphysics modelling software such as STAR-CCM + or COMSOL is more accessible and less computationally expensive in comparison to a fluidised-bed reactor. Therefore, most operations use fixed/packed-bed reactors for simulation. Dixon et al. [45] identified two primary approaches to simulating fixed bed reactors on computational fluid dynamics (CFD): both the porous medium model (PMM) and the particle-resolved CFD (PRCFD) have heavily been explored. The PMM approach operates on a macroscopic scale and is computationally less expensive than the PRCFD method, which resolves individual particles and behaves on a microscopic scale. Even though PMM is regarded as a prominent model due to its simplification in modelling, Dixon et al. [45] ensure that in the last decade, adequate progress and high interest have shifted toward the PRCFD approach due to its detailed intricacy.

Tong et al. [46] extensively explored the development of a simulation model for CMD using 65 wt% Ni-based catalysts in a 3D fixed bed reactor. Their primary objective was to perform a time-dependent study to analyse the concentration of hydrogen output and the catalyst deactivation rate under variable temperature and methane flow rate conditions. This simulation required kinetic modelling gathered from Zavarukhin et al. [35] and was applied to a packed porous catalyst, where methane gas underwent diffusion and chemical reactions. The simulation data obtained strongly correlated with experimental results across different temperatures, methane flow rates, and catalyst deactivation rate variations, thereby validating the simulation's accuracy. Consequently, by using the simulation model, future endeavours could focus on optimising the catalyst type to extend catalyst deactivation time. Tong et al. [46] also proposed the addition of catalyst regeneration mechanisms to the kinetics, potentially enhancing the economic benefits of CMD. While the availability of modelling papers on methane decomposition is limited, numerous modelling studies are available for SMR using fixed-bed reactors [47–54]. This abundance of modelling studies in SMR may be attributed to its well-established technology and widespread implementation in industrial hydrogen production.

Furthermore, it has been well-established that a fixed-bed reactor assesses and characterises the performance of a catalyst, making it ideal for laboratory applications. High conversion efficiency, reasonable temperature control, and ease of operation are among the key benefits of fixed-bed reactors [55]. Many researchers have conducted numerous experimental studies to enhance catalytic activity, stability, and other crucial catalyst characteristics. They utilise various characterisation technologies to examine conversion rates, selectivity, and product distribution under controlled conditions. Compared to fluidised-bed reactors, a fixed-bed reactor provides a more straightforward and less complex design since its functionality does not require an in-depth knowledge of fluid dynamics. The stationary catalyst in a fixed-bed reactor eliminates the challenges associated with fluidisation and particle mobility. Therefore, Muradov [56–60] have conducted multiple CMD studies using fixed-bed reactors, where different carbon morphologies and catalyst regeneration methods were critically evaluated.

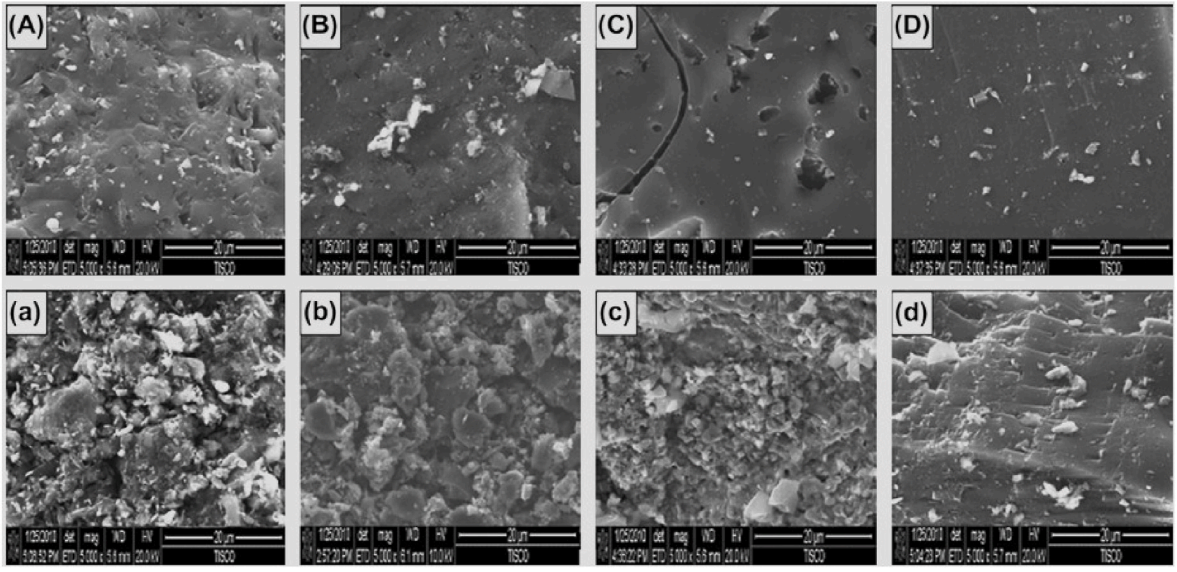

Fig. 5. SEM images of various chars before (A),(B),(C),(D) and after methane decomposition (a),(b),(c),(d) with a run time of 123 min (Used with permission from Ref. [40]. Copyright 2011, Elsevier).

This section will further familiarise readers with the current research methodologies required for catalyst characterisation. It will also emphasise the significance of fixed-bed reactors in conducting CDM experiments and preparing the catalyst types essential for characterisation.

3.1. Catalyst morphologies – SEM and TEM imaging

SEM is one of the most effective methods for visualising and examining the surfaces of micro- and nano-particle catalysts [61]. This imaging technique provides high-resolution visualisation of the catalyst's microstructure, offering fundamental information on topography, morphology, and composition [62]. As the electron beam is focused and accelerated through the catalyst material, a cascade of interactions occurs, emitting both photons and electrons [62]. The crucial role of electrons in scanning catalyst surfaces results in the development of high-resolution images. Consequently, SEM imaging plays a pivotal role in interpreting the complexities of catalyst microstructures, where catalytic properties and performance can now be visualised.

Wei et al. [40] conducted a comprehensive study using SEM images to determine the characteristics of different types of chars before and after CMD in a fixed-bed furnace. Upon analysing the SEM images, a significant accumulation of carbon deposits, visibly agglomerating the pores and surfaces, was observed after CMD, as depicted by the brighter appearance seen in Fig. 5a,(b),(c),(d) due to Z-contrast. On the other hand, prior to CMD, clean surfaces and sharp edges were observed (see Fig. 5A,(B),(C),(D)). Additionally, the superior catalytic activity of Shengli lignite (Fig. 5A) char was connected to its abundant pore count, outperforming other chars. This study also incorporated gas chromatography (GC) to quantify hydrogen yield and methane conversion rate after leaving the fixed-bed reactor. Notably, the hydrogen yield and methane conversion would decrease with time due to catalyst deactivation, as corroborated by the SEM images in Fig. 5. Overall, SEM imaging is a valuable instrument that provides a visualised interpretation of the diminishment in catalytic activity. Nevertheless, the ratio of agglomerated carbon on the catalyst surface cannot be quantitatively assessed using SEM images. Therefore, Suelves et al. [63] also employed X-ray photoelectron spectroscopy (XPS)- a surface technique to quantitively detect the amount of catalyst surface exposed to the encapsulating carbon.

Konieczny et al. [41] utilised SEM imaging to record the post-reaction state of Fe-based catalysts following fixed-bed reactor operation. Their findings demonstrated two distinct carbon morphology types during methane decomposition reactions: plate-like structures and nanofibers. According to the SEM imaging, the carbon deposition obstructed the active sites, hence diminishing the catalytic activity. Konieczny et al. [41] investigated the preparation and application of Fe-based catalysts for methane decomposition, aiming to achieve complete CDM over extended time intervals (>75 h). In this case, the fixed-bed reactor fulfilled dual purposes: initially preparing the Fe-based catalyst from iron oxide using elevated temperatures and atmospheric pressure, followed by the subsequent CDM. They compared catalyst activation pre-treatment using two reacting gases (H_2 and CH_4) at three temperatures (800, 850, and 900 °C). Notably, methane at 900 °C was favoured and chosen due to its shorter preparation time of approx. 2 h. While a fixed-bed reactor is well recognised as ideal for CDM, experimental studies have revealed that it also plays a significant role in catalyst preparation. These reactors are essential in transforming precursor materials into activated catalytic species, achieving desired structural and morphological properties. Furthermore, similar to

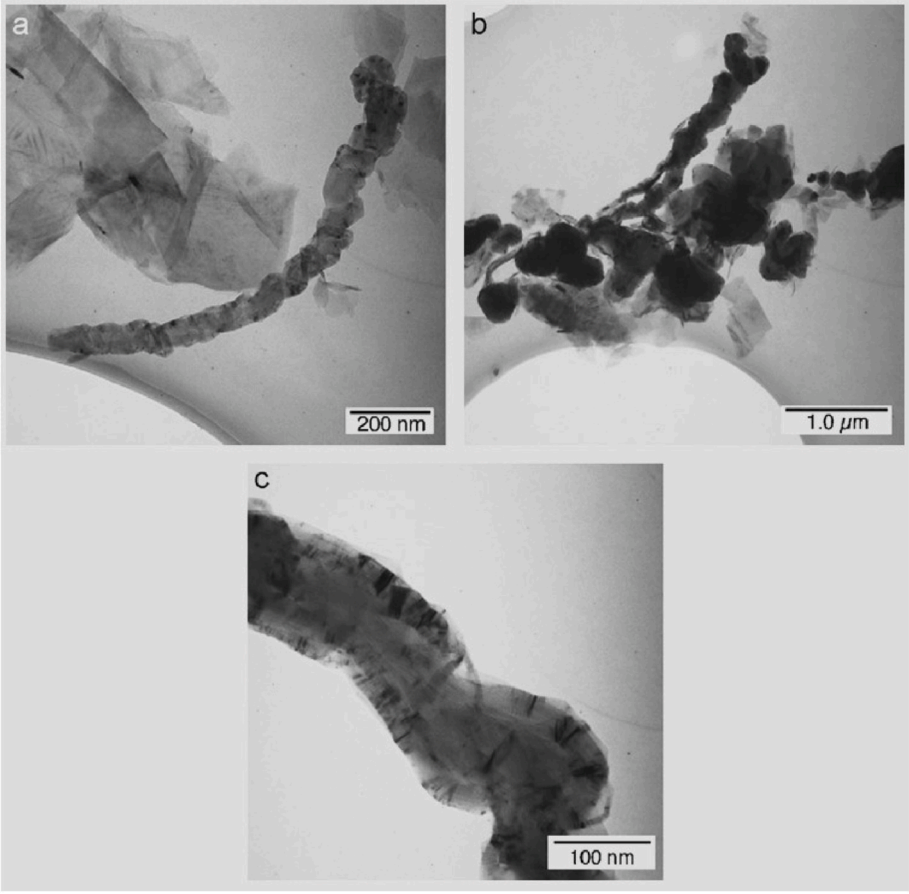

Fig. 6. TEM imaging to analyse the nanofibers agglomerated around the catalyst surface. (Used with permission from Ref. [41]. Copyright 2008, Elsevier).

Konieczny et al. [41], the utilisation of fixed-bed reactors allows researchers to thoroughly investigate various catalyst formulations, compositions, and activation methods.

Additionally, TEM imaging (Fig. 6) by Konieczny et al. [41] at 10, 000× magnification provided finer details of the structural morphologies of carbon nano-fibre coating the Fe-based catalyst surface post-methane decomposition. These TEM pictures (Fig. 6) highlighted the unique shape of the carbon nanofibers, resembling linear plates interconnected end to end to form fibrous structures. The sizes of the elliptical shapes collected from TEM ranged between 610 nm and 1 m and are in agreement with data found in the SEM photomicrographs. However, according to Bayat et al. [64], it is impossible to accurately determine the precise length of nanofibers due to their intertwined nature; hence, estimations are usually made.

Yang et al. [65] explored the catalytic performance of carbon-based catalysts (AC, CB, and AC-CB combinations) in CMD using a bench-scale fixed-bed configuration. High-resolution TEM was employed to examine the structural morphology of carbon deposited on activated carbon (AC), carbon black (CB), and the $AC_{0.5}$-$CB_{0.5}$ mixture. Yang et al. [65] used an enhanced resolution to reveal a graphene-like filamentous layer, with depositions displaying interplanar structures almost parallel to the carbon catalyst backbone. Compared to AC, the graphene growth layers on CB and $AC_{0.5}CB_{0.5}$ mixture contained more highly curved structures, implying that deposited carbon could cause more structural defects, resulting in a less ordered system and consequently prone to maintain or improve CMD. Therefore, the TEM images provided support for previously reported findings, including data from BET and kinetic performance, which validated the catalyst stability of CB > AC during CMD.

While morphological changes may be visualised and surface information can be obtained through SEM and TEM, X-ray diffraction analysis (XRD) primarily determines crystal structure and phase composition. Most experimental reports usually aim to combine SEM, TEM and XRD to gain a comprehensive understanding of the behaviour of the catalyst, including changes in surface morphology and crystallography during the CMD [63,64,66–72]. The following section will further explore XRD analysis.

3.2. Chemical composition – XRD analysis

A non-destructive method known as XRD offers comprehensive information on a material's crystallographic structure, chemical composition, and physical characteristics [73–75]. In XRD, the produced X-rays are collimated and directed at a sample of nanomaterials. The interaction of the incident rays with the sample results in a diffracted pattern, which is then detected, processed, and counted. A diffraction pattern is shown by plotting the intensity of the diffracted rays that are dispersed over the material at various angles [73]. Numerous experimental studies have utilised fixed-bed reactors and employed XRD techniques to characterise both fresh and deactivated catalysts [41,57,63,64,66–72,76–78]:

Suelves et al. [63] developed a fixed-bed reactor intending to achieve successful CMD by producing CO-free hydrogen. The experiment was conducted by employing a commercial Ni-based catalyst to investigate the characteristics of the generated carbon. The structural properties, including crystallinity, of the fresh catalyst load were assessed using XRD. Before the activity testing, Suelves et al. [63] had performed a reduction treatment on the catalysts. This involved processing pure H_2 at a flow rate of 20 ml/min for 3 h at temperatures of 550 and 650 °C. This pretreatment was essential because the XRD examination revealed that 4 wt% of the Ni from the fresh catalyst was detected as NiO (see Table 1). Therefore, utilising XRD on the fresh catalyst load minimises impurity accumulation and enhances catalytic behaviour during the methane decomposition reaction. Similarly, Ramasubramanian et al. [69] also characterised the prepared catalyst using XRD patterns, revealing the presence of Fe_2O_3, Co_3O_4 and MoO_3 phases found in the freshly calcined catalyst (see Fig. 7a for interpretation). Subsequently, after reducing the catalyst using an H_2/N_2 mixture at 700 °C, a follow-up XRD analysis was approached, showing the complete reduction of metal oxide phases to its elemental form of Fe, Mo and Fe–Co alloys (see Fig. 7b). This XRD interpretation is necessary for detecting an oxidised catalyst, and processing reduction is essential when optimising/maximising the catalyst's activity, selectivity, and stability.

3.2.1. Characterisation of spent Catalyst

In a further study, Suelves et al. [63] harnessed XRD patterns to investigate the deactivation of catalysts. XRD patterns can offer important insights into the alterations in the catalyst's crystallinity and structure that occur during the CMD process. As illustrated in Fig. 8, there is an additional intense reflection (0 0 2) at 26.2° across all 8 diffraction patterns, featuring a basal interplanar distance of 0.335 nm. This observation conveys the presence of graphitic carbonaceous species coating on the catalyst surface, affecting both their activity and selectivity. The relative definition of the peak attributed to carbon (26.2°) intensifies in the XRD patterns, with higher levels of carbon deposition, though no structure differential was detected. Ramasubramanian et al. [69] also drew a similar interpretation when analysing Fe-based catalyst (Fe–Mo/$CeZrO_2$). A supplementary XRD peak was observed on the spent catalyst at $2\Theta = 26.56$ ° in all the spectra, implicating the agglomerating of graphitic carbon on the catalyst's active site.

Moreover, Suelves et al. [63] presented Table 2, signifying the XRD analysis of the Ni-based catalyst after the decomposition reaction. In comparison to Table 1 above (outcomes from fresh catalyst), it is evident that the deactivated sample exhibited a larger crystalline domain size within the Ni. This implies Ni is undergoing thermal sintering, where the catalyst lifetime is shortened at higher temperatures. In this context, the elemental carbon by-product encapsulates the active sites, leading to an increase in the crystalline domain size. This would ultimately result in fewer accessible active sites for the reactant due to the reduction of the overall available surface area.

Lastly, Suelves et al. [66] also conducted a parallel investigation using the same fixed-bed apparatus, focusing this time on characterising a carbon-based catalyst. The experimental pattern reported was similar to that of the Ni-based catalyst [63], where the XRD study revealed that catalyst deactivation is not associated with a differential in structural changes; however, it is related to the loss in surface area during CMD. Moreover, Yang et al. [65] investigated a carbon-based catalyst (AC, CB and AC-CB mixture), where initially before the reaction, a broad peak at $2\theta = 24°$ was observed, illustrating the amorphous carbon structure. However, post CMD, a sharp peak at $2\theta = 26°$ was detected, mirroring observation made by Suelves et al. [63], who had examined metal-based catalysts. This detected peak comprised an ordered graphitic coating that was deposited on the catalyst surface during methane decomposition. Yang et al. [65] proceeded to quantitatively compare the different catalysts by analysing the different intensities at $2\theta = 26°$ (see Fig. 9).

Table 1
The structural properties of fresh Ni catalyst determined using XRD (Used with permission from Ref. [63]. Copyright 2005, Elsevier).

Samples	Ni (Nickel)			NiO (Nicke Oxide)		
	Composition (wt%)	a (nm)	Size (nm)	Composition (wt%)	a (nm)	Size (nm)
Ni	96	0.352	5	4	0.417	13
Ni pre-reduced	95	0.353	7	5	0.418	5

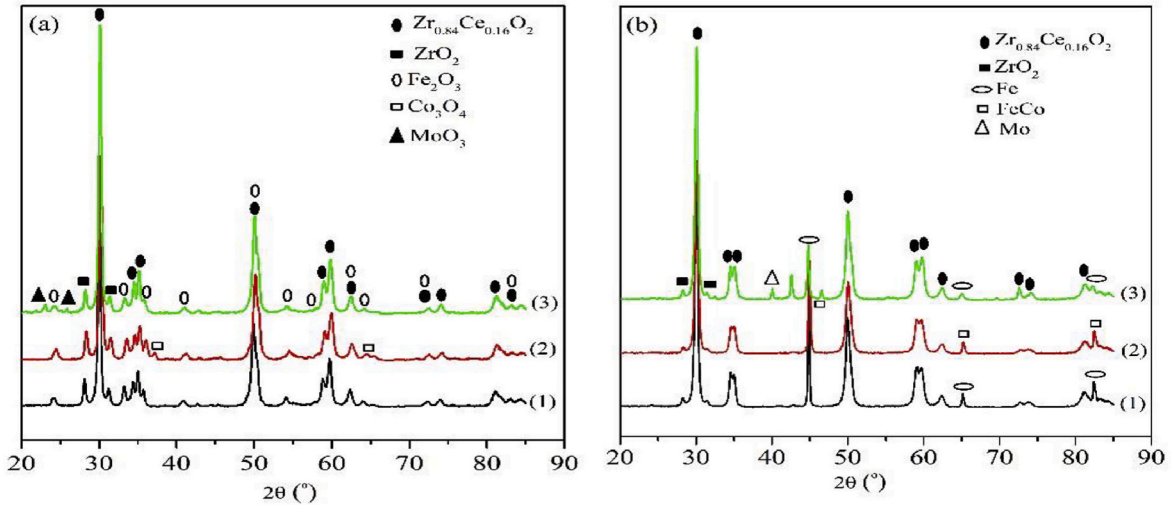

Fig. 7. XRD pattern of (a) fresh catalyst load and (b) complete reduction of metal oxide phase. (Used with permission from Ref. [69]. Copyright 2020, Elsevier).

Greater intensities meant the catalyst possessed a higher degree of structural order due to the deposited carbon. As depicted in Fig. 9, the $AC_{0.5} - CB_{0.5}$ mixture displayed the greatest intensity at $2\theta = 26°$.

Overall, XRD is a valuable characterisation method for investigating the crystallographic properties of catalyst materials before and after methane decomposition. This allows researchers to understand and compare the behaviour and efficiency of the catalyst. However, many experimental reports aim to utilise multiple characterisation methods like SEM, TEM, Brunauer-Emmett-Teller (BET), Thermogravimetric Analysis (TGA) and Raman Spectroscopy in order to complement the XRD patterns and provide a more thorough understanding of the structure, morphology and composition of the catalyst.

3.3. Surface area and pore structure – BET analysis

The Brunauer-Emmett-Teller (BET) theory serves as a key analytical tool for determining and calculating the specific surface area, pore volume and distribution of the catalyst [79–81]. It relies on nitrogen adsorption isotherm measurements at 77 K to explain the physical adsorption of gas molecules on a solid surface [81]. Given the known influence of surface area and pore structure on catalytic performance, methane decomposition reactions often involve measuring N_2 BET surface areas before and after the reaction.

3.3.1. Catalyst textural properties

Mahmoodzade et al. [82] conducted CMD in a continuous fixed-bed quartz reactor under atmospheric pressure. This study involved a series of Ni-based catalysts with various loading (25, 40, 55, and 70 wt%) onto the spherical mesoporous SiO_2 support. Initially, untreated SiO_2 support exhibited a large BET area, small average pore size, and high pore volume, facilitating excellent dispersion of Ni when doped. However, according to Table 3, the specific surface area and pore volume of the catalyst support were significantly reduced when high-content nickel was added. This is attributed to the agglomeration and production of NiO clusters that result in partial blocking of the micropores and eventually degradation of the pore structure upon impregnation, drying and calcination steps. Therefore, BET characterisation revealed a diminishing BET area with increasing nickel content on the support (see Table 3). After using BET and several other characterisation methods, the study concluded that the preparation of 55 wt% Ni/SiO_2 provided the optimal performance with a high methane conversion of 54% at 575 °C when compared to other catalyst types. This study's approach was to use BET characterisation to confirm the best catalyst to support composition when maximising the methane conversion rate.

Likewise, Bayat et al. [64] managed a quartz fixed bed micro-reactor to simultaneously synthesise COx-free hydrogen and carbon nanofibers via CMD. The catalytic behaviour of $Ni–Fe/Al_2O_3$ catalysts with different Fe content was examined. According to the findings, adding Ni and Fe to the Al_2O_3 support led to a reduction in BET surface area and pore volume. This is due to the partial blockage of alumina pores by nickel and iron oxide clusters, aligning with the conclusion drawn by Mahmoodzade et al. [82]. The two studies portray that clusters of catalyst oxide become larger than the pores of the support; hence, this reduces the accessibility of methane reactant during the decomposition process, encouraging the sintering of catalyst.

On the other hand, the following papers from Ramasubramanian et al. [69], Pinilla et al. [83] and Pudukudy et al. [84] had contrasting viewpoints when exploring the catalyst's textural property using BET. All the studies mentioned here utilised a fixed-bed quartz reactor to handle the CMD reaction. Ramasubramanian et al. [69] reported that the iron-impregnated catalyst had a larger surface area when compared to the pure support material. Moreover, the inclusion of a promoter metal further enhanced the surface area of the catalyst, as depicted in Table 4. The impregnated metal precursors create nanoparticles on the support material, increasing active sites' availability and enhancing the accessible surface area for reactions. This leads to an increased BET surface area, a key measure of the material's accessibility. Additionally, Pinilla et al. [83] encountered a similar outcome to Ramasubramanian et al. [69], where the specific surface area of Fe/Al_2O_3 (catalyst on support) and $FeMo/Al_2O_3$ (including the promoter) had a significant incline in comparison to the pure support material. Lastly, in a comparative study, Pudukudy et al. [84] found that the BET surface area of the unpromoted Ni catalyst and Pd-promoted catalyst was 22.63 m^2/g and 29.38 m^2/g, respectively. Therefore, this signifies the crucial role of textural promoters when improving the 'catalytic activity, hydrogen yield, and methane conversion' [26]. Considering the fast deactivation that occurs with Ni- and Fe-based catalysts through encapsulation, promoters play a crucial role in dispersing and stabilizing the catalyst particles on the support [26,85]. This enhanced dispersion expands the surface area of the catalyst available for reaction, allowing for more efficient interaction between methane molecules and catalytic sites through diffusion.

Additionally, several studies have explored the textural characterisation of fresh and deactivated catalysts, which were accompanied by the use of fixed-bed reactor [65,86]. Liu et al. [86] assessed the catalytic performance of AC and CB for methane thermo-catalytic cracking by utilising a bench-scale fixed-bed setup. The collected data on 'BET N_2 surface areas, average pore width and pore volumes' was correlated

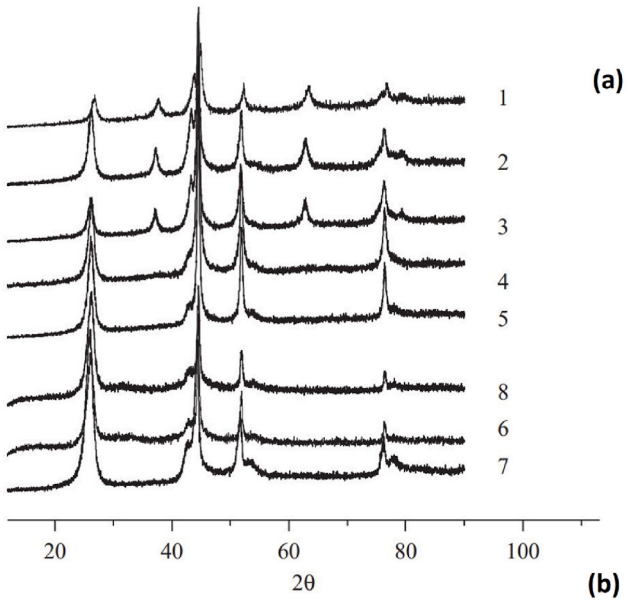

Fig. 8. (a) XRD pattern of spent Ni catalyst and (b) variety of reaction conditions listed (1-8) (Used with permission from Ref. [63]. Copyright 2005, Elsevier).

Table 2
XRD study on the spent catalyst that shows an increase in crystalline domain size for 7 samples (Used with permission from Ref. [63]. Copyright 2005, Elsevier).

Samples	Composition (wt%)			Graphite Cell (nm)			Ni Cell (nm)	
1	22	25	53	0.250	0.679	8.5	0.350	8.9
2	16	14	70	0.246	0.679	10.6	0.352	13.7
3	30	18	52	0.244	0.682	8.1	0.352	12.7
4	27	–	73	0.246	0.680	7.9	0.353	14.3
5	18	–	82	0.246	0.682	17.4	0.353	18.4
6	9	–	91	0.245	0.676	12.0	0.351	16.0
7	8	–	92	0.246	0.684	9.5	0.353	50.0

with the literature. Initially, as seen in Table 5, AC-B had the largest BET surface area of 920.2 m^2/g and the smallest pore width (3.0 nm), which was to be expected, as it has been reported from literature studies that AC provides the highest initial activity [56]. However, after 6 h of CDM at 900 °C, the AC (AC-900) BET surface area dropped tremendously to 1.7 m [2]/g, its pore volume was almost zero, and its average pore width

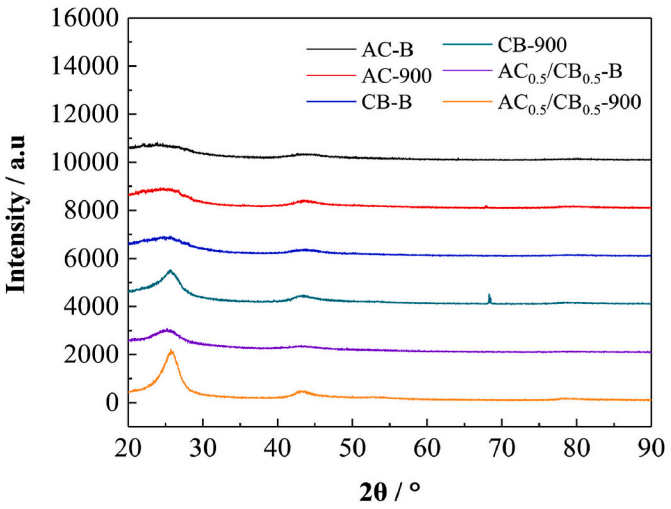

Fig. 9. Quantitative comparison of XRD patterns between AC, CB and $AC_{0.5}$ – $CB_{0.5}$ after methane decomposition. (Used with permission from Ref. [65]. Copyright 2020, Elsevier).

Table 3
Characteristics of catalysts with various loading % of support collected using BET instrumentation. (Used with permission from Ref. [82]. Copyright 2020, Elsevier).

Samples	Surface area (m [2]/g)		Pore volume (cm [3]/g)		Pore size (nm)	
	Fresh	Spent	Fresh	Spent	Fresh	Spent
SiO_2	1136.0	–	1.21	–	4.2	–
25%Ni/SiO_2	725.7	25.4	0.66	0.05	3.5	7.6
40%Ni/SiO_2	529.6	131.1	0.40	0.2	3.0	7.3
55%Ni/SiO_2	388.2	100.4	0.44	0.3	4.5	13.5
70%Ni/SiO_2	225.0	54.3	0.19	0.15	3.3	11.0

Table 4
Effect of BET surface area, pore volume and pore diameter when promoted metals are incorporated into catalyst with support. (Used with permission from Ref. [69]. Copyright 2020, Elsevier).

Catalysts	Surface area (m^2/g)	Pore volume (cc/g)	Pore diameter (nm)
Fe/$CeZrO_2$	13.03	0.15	3.81
Fe–Co/$CeZrO_2$	19.97	0.11	3.81
Fe–Mo/$CeZrO_2$	24.08	0.12	3.81

Table 5
Comparative analysis of the Surface area and porosity between AC and CB. (Taken from the source without modification) . (Used with permission from Ref. [86]. Copyright 2018, Elsevier).

Catalysts	BET Surface Area (m^2/g)	Average Pore Width (nm)	Pore Volume (cm^3/g)
AC-B	920.2	3.0	0.08
AC-900	1.7	10.5	0.006
CB-B	84.8	13.5	0.27
CB-900	83.0	16.7	0.33

grew to 10.5 nm. These observations suggested the blockage of micro-pores from deposited encapsulating carbon, resulting in the quick deactivation of the catalyst. Similarly, Bai et al. [87] investigated CMD on three different compositions of AC, where the BET surface area was drastically reduced after 2 h at 1123K, paralleling the findings of Liu et al. [86]. Conversely, Liu et al. [86] also examined CB catalyst, which exhibited minor changes in the BET surface area (84.8 to 83.0 m^2/g),

pore volume (0.27 to 0.33 m^3/g), and average pore width (13.5 to 16.5 nm) during the 6h interval of the reaction showing its remarkable stability/ durability during CMD.

As evident, BET is a widely used technology for studying the textural properties of both fresh and deactivated catalysts. However, BET alone as a characterisation technique comes with some limitations when incorporated into CMD. According to Lopez et al. [88], the physical surface concentration of the catalyst may vary depending on the catalytic composition, surface chemistry and structure; hence, it is unlikely that the catalytic performance would be strongly associated with BET surface area. As previously observed by Liu et al. [86] , the BET surface area measurement provides an overall estimate of the accessible active sites; it does not reflect the actual distribution or abundance of these sites, significantly influencing the catalytic activity. In order to address these drawbacks, it is critical to use various characterisation methods like spectroscopy, imaging, TGA, GC-MS and kinetic studies. Combining these methodologies can help better interpret the catalytic activity, selectivity and stability.

3.4. Thermogravimetric Analysis (TGA)

Typically, thermogravimetric studies (TGA) have evolved into a cost-effective, faster, and simpler analytical tool for identifying and analysing the thermal stability, purity, and mass of carbonaceous deposits on the catalyst surface during CMD [69,89–102]. TGA is primarily utilised to characterise the morphologies of carbon deposits on active sites, although various other studies have explored its application in CMD reactions. The primary purpose of TGA is to subject the catalyst sample to rising temperatures to measure the weight change, providing data on the spent catalyst's composition and thermal behaviour [90,91].

Ahmed et al. [90] work involved managing a fixed-bed reactor under conditions of 700 °C, where bimetallic Ni–Mo catalysts were studied, and a comparison between CeO_2 and CeO_2–SiO_2 supports was conducted. TGA measures the sample's weight loss as a function of temperature and time [91]. Both catalyst types showed a similar trend, with no weight loss below 500 °C, signifying the absence of amorphous carbon. Weight loss began at approximately 520 °C due to removing water vapour at high temperatures, followed by the coke deposition further degrading the catalyst and ending beyond 600 °C. Additionally, the weight loss is directly in conjunction with the amount of methane decomposed, where the greater hydrogen yield is directly associated with the higher carbon yield. Therefore, according to data from Ahmed et al. [90], the catalyst Ni–Mo/CeO_2 displayed a higher carbon generation than the Ni–Mo/CeO_2–SiO_2. These findings demonstrate that the addition of SiO_2 inhibits the catalytic activity and are extremely congruent with the TEM and Raman-Spectroscopy findings. Collectively, these studies from Refs. [90,93,98] show that the TGA data are consistent with other analytical techniques such as TEM, XRD, and Raman Spectroscopy measurements.

Furthermore, Torres et al. [103], Ibrahim et al. [94] and Fakeeha et al. [92] considered the analysis of Fe-based catalysts by employing the TGA technique. Torres et al. [103] examined Fe-based catalysts, incorporating MgO and Al_2O_3 as textural promoters, with some samples doped with Mo. The data portrayed that the loading of Mo on a catalyst prepared with Al_2O_3 had the best catalytic activity due to its highest carbon accumulation yield. Therefore, TGA analysis allows for the identification of the most effective promoters to enhance the catalytic performance during CMD. Additionally, Ibrahim et al. [94] attempted to use a fixed-bed flow reactor at 700 °C to undergo CMD using a Fe-based catalyst. The weight loss profile caused by heating is illustrated in Fig. 10. The removal of water vapour and carbonaceous species that had developed on the spent catalyst is what caused the successive weight loss, where TGA curves levelled off at 640 °C, 650 °C and 770 °C for 20% Fe/Al_2O_3, 40% Fe/Al_2O_3 and 80% Fe/Al_2O_3 respectively. The data confirms that 100% Fe performed the worst weight loss, explaining the significance of catalyst support when maximising the catalyst's performance, stability and selectivity. TGA is a valuable tool when interpreting the optimal catalyst support and dopant by determining the thermal stability (observing the weight gain or loss), identification/ quantification of adsorbed species, and characterising the porosity (SA and dispersion).

Fakeeha et al. [92] took a distinct approach when using TGA in comparison to Torres et al. [103] and Ibrahim et al. [94]. Instead of finding the best catalyst support or promoter, the aim was to distinguish the best-calcined temperature for 20% Fe/Al_2O_3 catalyst ranging between 300 and 800 °C, as well as the most effective method for catalyst preparation: impregnation or co-precipitation. Again, the TGA measurements were conducted on the spent catalyst, where the optimum calcination temperature was found to be 500 °C for both impregnated and co-precipitated catalysts. Moreover, the data also confirmed that the co-precipitation catalyst produced more carbon per mole of methane converted compared to the impregnation catalyst. This signifies that different calcination temperatures would alter the textural properties of the catalyst; hence, TGA quantification helps determine the best

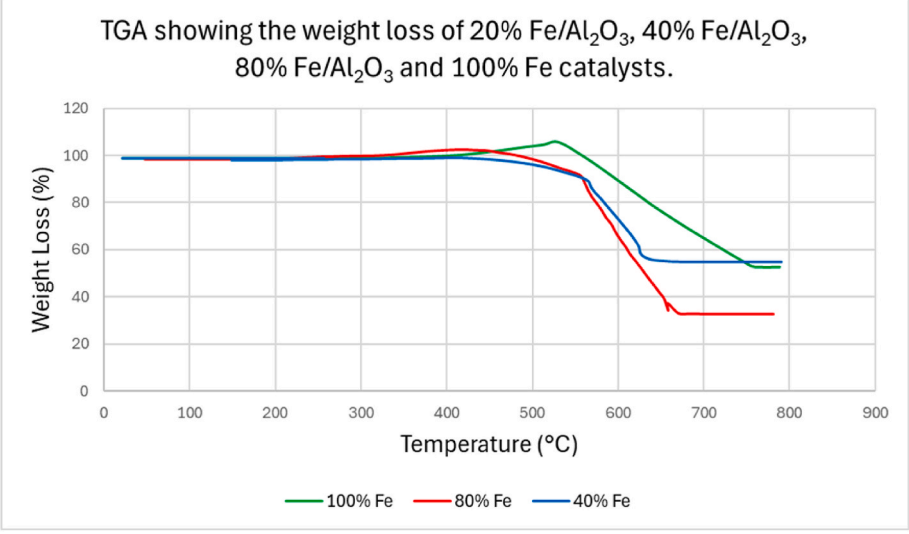

Fig. 10. TGA showing the weight loss of 20% Fe/Al_2O_3, 40% Fe/Al_2O_3, 80% Fe/Al_2O_3 and 100% Fe catalysts. (Used with permission from Ref. [94]. Copyright 2015, Elsevier).

calcination temperature required for CMD.

Overall, the extensive use of fixed-bed reactors with the characterisation analysis of TGA in catalysis research has resulted in the measurement and understanding of carbon deposition on catalytic active sites. The potential for optimising the catalyst support type and enhancing regeneration steps is significant, thus playing a crucial role in advancing CMD.

4. Fluidised-bed reactors

Fluidised-bed reactors are the most widely known configuration utilised on laboratory and industrial scales [104]. Their adaptability covers a wide range of industries, including the petroleum, chemical processing industry, fuel and mineral processing, and waste treatment [104,105]. Fluidised-bed reactors outperform fixed-bed reactors in several crucial areas, such as promoting vigorous mixing of catalyst particles with the fluid and improving mass and heat transfer while lowering temperature gradients inside the reactor [106–108]. Due to the fluidised-bed reactor's dynamic behaviour, hot spots—commonly seen in fixed-bed reactors from immobilised catalyst particles—can be successfully managed and kept at a constant temperature across the bed [107]. In addition, the loading and unloading of catalysts in a fixed-bed reactor is time-consuming, and, from an industrial standpoint, this will be costly on a large scale [107]. Fluidised-bed reactors, on the other hand, enable continuous CMD by mobilising fresh catalyst particles while periodically withdrawing spent ones. This seamless catalyst management minimises carbon clogging and considerably improves system efficiency [106–108]. An example of an experimental fluidised-bed reactor is shown in Fig. 11, where multiple parameters are explored in order to optimise the system [109].

An insightful study by Qian et al. [110] examined the catalytic activity and stability of a 40 wt% Fe/Al_2O_3 between a fluidised-bed reactor and a fixed-bed reactor under atmospheric pressure. Both reactors initially attained a steady methane conversion of 53%. However, the

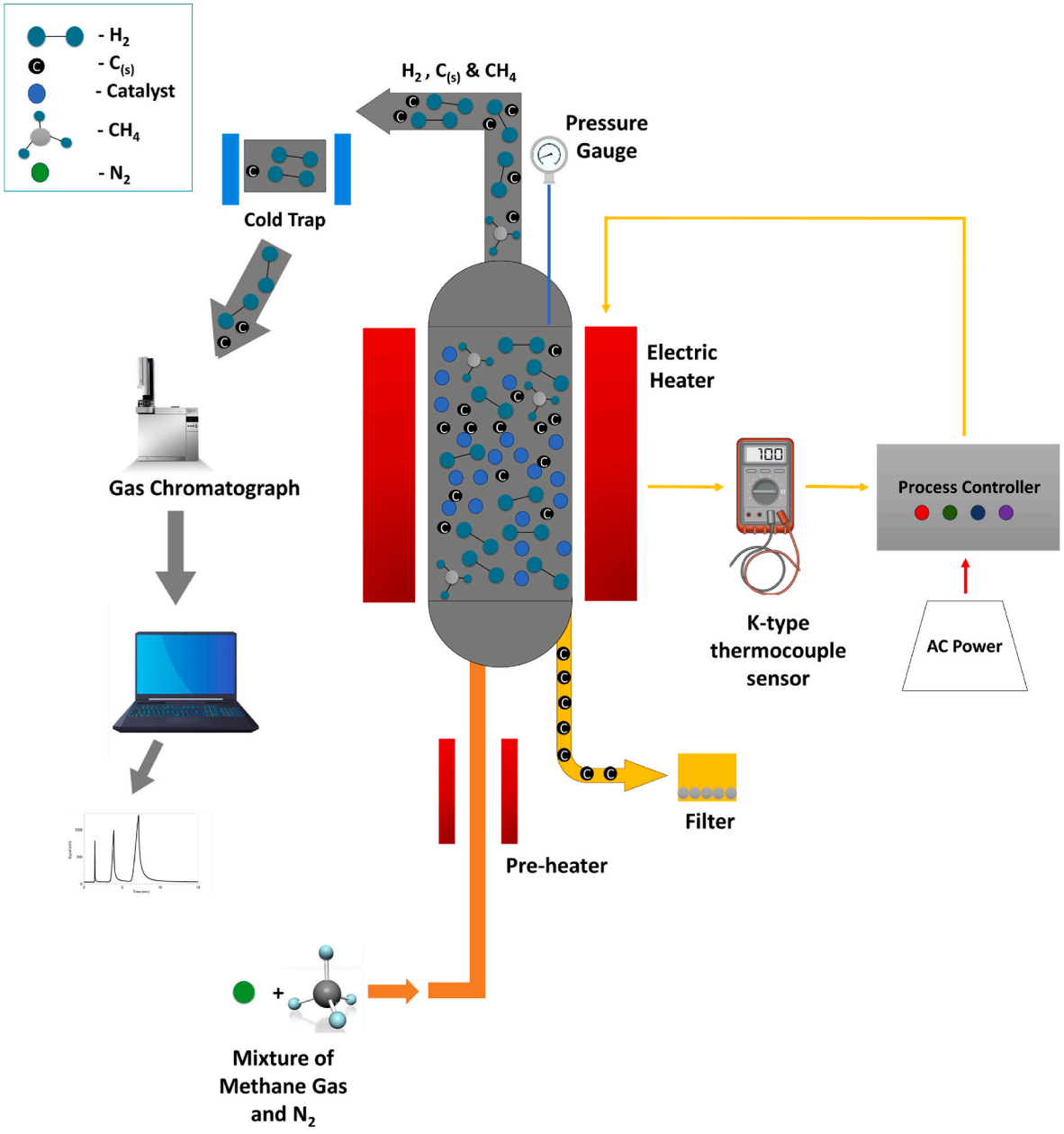

Fig. 11. An experimental set-up that utilises a fluidised-bed reactor to conduct catalytic methane decomposition reaction. (For a more precise understanding, please refer to the key in the top left corner, which highlights the components represented in the figure).

conversion rate of the fluidised-bed reactor decreased over time and reached 47% after 35 min as opposed to 20 min for the fixed-bed reactor to attain the same level. The fixed-bed reactor had an exponential pressure drop, reaching 400 mbar in 35 min and finally forcing the reactor to shut down, but the fluidised-bed reactor showed a slower fall in pressure. The fluidised-bed reactor's exceptional efficiency was further shown by the fact that it outperformed the fixed-bed reactor by continuing CMD for up to 60 min. This study supports the effectiveness and dependability of the fluidised-bed reactor in processing CMD.

The functionality of a fluidised bed involves introducing the gas stream that circulates across the bed at a high velocity and mixes intimately with the solid catalytic particles – Fig. 11. The solid particles are suspended in the emulsion phase by the upward flow of the reacting gas within the fluidised-bed reactor, giving the mixture fluid-like characteristics [111–113]. As a result, fluidised bed reactors are highly favoured since they promote excellent mixing and offer a wider surface area for the reaction to occur [114]. Specific configurations are particularly advantageous due to their rapid heating rate, homogeneous heat distribution, efficient mass transfer, and reasonable control of the reaction parameters [112]. However, there are some fundamental limitations of fluidised-bed reactors [115]. Firstly, there are challenges in scaling up the reactor due to complications of moving from a small laboratory-scale to a big industrial-scale reactor. As will be seen in due course, no mass transfer limitations exist on a laboratory scale. Nevertheless, the design and scaling-up of large-diameter reactors remain unpredictable due to mass transfer limitations occurring in most fluidised bed processes, especially within the bubbling and turbulent regime [113,115]. Therefore, these restrictions may significantly impact the conversion rate and total reactor efficiency.

Despite these limitations, in recent years, tremendous progress has been achieved in fluidised-bed reactor research and development. Researchers are actively investigating the many hydrodynamic systems within reactors to address scaling concerns and improve performance. There is a particular emphasis on researching both experimental and industrial uses of fluidised-bed reactors to improve their operation and maximise their potential. In this review paper, we shall comprehensively assess the numerous hydrodynamic systems of fluidised-bed reactors, providing insight into the complexities of their behaviour. In addition, we will thoroughly examine the practical uses of fluidised-bed reactors in both experimental and industrial settings. We hope to unleash the full potential of fluidised-bed reactors and promote improvements in their application across a variety of industries by resolving the issues and comprehending the entire range of their performance.

4.1. Temperature control

As already discussed, fluidised bed reactors offer numerous fundamental advantages, with one of the most significant being excellent heat transfer and temperature uniformity across the bed [116]. However, to fully realise these advantages, researchers must first discover the optimal temperature for a specific fluidised bed structure and catalytic type. High temperatures are often necessary to achieve a high methane conversion rate, as the temperature strongly influences the reaction kinetics and the overall performance [113]. Therefore, we will examine experimental literature involving different catalyst types in a fluidised bed reactor to identify the most suitable operating temperature. Through this analysis, we aim to identify the specific goal and methodology employed in each experimental study.

Generally, transition-metal (Fe, Ni, and Co)-based catalysts are extensively used in CMD processes, operating at moderate temperatures typically ranging from 500 to 800 °C [8]. Fe-based catalysts have received significant attention in recent years due to their improved performance, particularly when operated at higher temperatures within the suggested range. At high temperatures, Fe-based catalysts are preferred due to their higher efficiency and selectivity in CMD processes.

Torres et al. [117] specifically worked on a Fe/Al_2O_3 catalyst that underwent CMD using a fluidised bed reactor. The aim was to distinguish the operational conditions, such as reaction temperature and space velocity, that heavily influence the methane conversion rate. Regarding the temperature study, Fig. 12 illustrates the methane conversion at various reaction temperatures (ranging between 700 and 900 °C) using a methane flow rate close to U_{mf} (analysed in section 4.2.1). At 700 °C, the methane conversion rate was the lowest at 15%. As the temperature increased to 900 °C, the initial methane conversion rate after 15 min reached 68%. However, the catalyst deactivation at higher temperatures was more prominent, as according to Hou et al. [118], higher temperatures result in the excessive production of carbon, resulting in quicker deactivation from the encapsulation of filamentous carbon. When the methane conversion curves in Fig. 12 were examined, optimum catalyst performance appeared around 800 °C, establishing a balance between a relatively high initial reaction rate and sustained activity.

In contrast to a metal-based catalyst, a carbon catalyst generally exhibits lower catalytic activity, requiring a higher operating temperature of 800–1000 °C [21]. Nevertheless, despite these difficulties, carbon-based catalysts have gathered significant attention from the scientific communities due to their advantageous characteristics that outweigh the drawbacks of a metal catalyst. Notably, carbon catalysts have great endurance to high temperatures, which makes them more suitable for use in fluidised-bed reactors at industrial scales [21].

Jung et al. [119] investigated CMD on activated carbon and carbon black within a fluidised-bed reactor. This process was conducted across a temperature range of 800–925 °C. Initially, the activated carbon exhibited higher activity than carbon black. However, a consistent trend of rapid deactivation was observed for activated carbon across all reaction temperatures. This suggests that activated carbon's susceptibility to quick deactivation is attributed to filament carbon encapsulation. On the other hand, the carbon black commenced with lower initial activity; however, the catalytic performance reached a quasi-steady state and remained consistent for over 8 h, irrespective of the reaction temperatures. Comparatively, the initial activity of the activated carbon catalyst was <40%, which was still lower than the initial activity of 68% of the Fe/Al_2O_3 catalyst (as reported in Torres et al. [117]). Conversely, carbon black maintained a higher methane conversion rate of >20% during its 8 h interval at an optimal temperature of 925 °C. This contrasts with the findings of Torres et al. [117], where conversion remained below 20% after the 6 h mark. These observations demonstrate the remarkable durability of carbon black in comparison to both activated carbon and Fe-based catalysts.

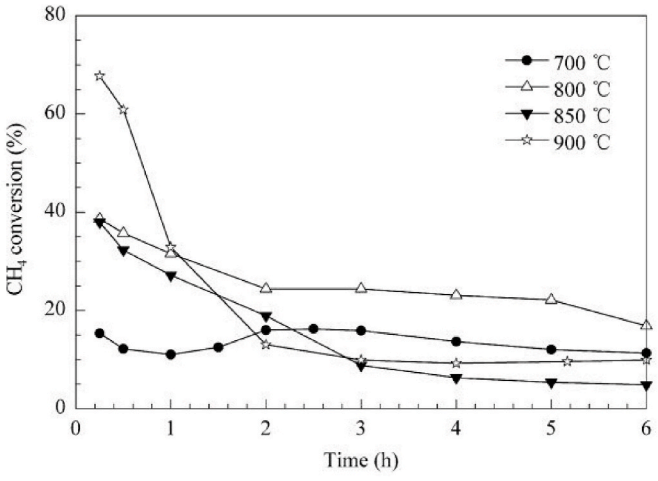

Fig. 12. Methane conversion at temperatures between 700 and 900 °C at WHSV: 6 $L_N/(g_{cat}.h)$. (Used with permission from Ref. [117]. Copyright 2012, Elsevier).

4.2. Methane velocity in a fluidised-bed reactor

As the flow rate of methane gas through the catalytic bed increases incrementally, the gas would initially flow through the void spaces between the stationary particles, showing characteristics of a fixed-bed reactor [120]. However, as the flow rate of methane gas increases, the particles start migrating into restricted regions, leading to increased voidage and the formation of an expanded bed. Eventually, at a velocity surpassing minimum fluidisation velocity (U_{mf}), all the particles are simply suspended by the upward-flowing gas, as the stability of close-packing is lost [113,120]. In the fluidised state, the gas's upward frictional drag force on the catalytic particles equally counterbalances their apparent weight; that is, the actual weight less than the buoyancy force, therefore allowing particles to be suspended with the fluid. [113,121].

At U_{mf}, the pressure drop is just enough to maintain the particles' submerged weight, resulting in catalytic particles being freely suspended by the fluid (incipient fluidisation) rather than resting on nearby particles; hence, the bed is considered as fluidised [120,122,123]. U_{mf} could vary depending on the particles' size, shape, density and Geldart group, as well as the density and viscosity of the gas [124]. Usually, the pressure drop as a function of gas velocity is often measured experimentally to ascertain the value of U_{mf} [125]. More specifically, when particle size and density rise, so does the U_{mf} [30].

4.2.1. Experimental classification of U_{mf}

An experimental investigation is essential when estimating the U_{mf}, a fundamental parameter necessary for fluidised-bed reactor development. Amin et al. [106] and Allaedini et al. [126] independently conducted their experimental research on measuring the U_{mf} in the context of CMD. This technique was first proposed by Pinilla et al. [109,127].

Pinilla et al. [109,127] conducted two distinct studies using a $NiCu/Al_2O_3$ catalyst to assess the pressure drop across a vertical pilot-scale fluidised bed. These studies investigated the experimental outcome when increasing superficial velocities while co-currently monitoring the time-mean pressure drop [128]. Other parameters, such as temperature, remained constant at 700 °C. To distinguish the U_{mf} empirically, employing inert nitrogen gas rather than methane was recommended. Consequently, the velocity determined using nitrogen was multiplicatively adjusted by a factor of 1.4 to account for the influence of methane. Fig. 13 illustrates the experimental results visually, demonstrating the link between ΔP and the superficial gas velocities.

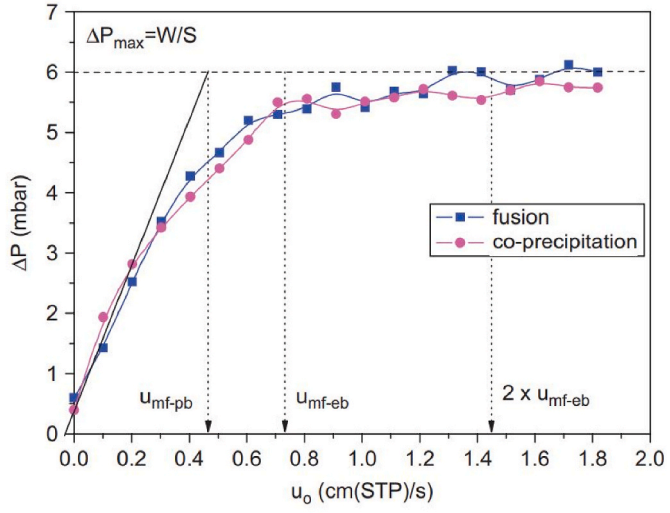

Fig. 13. The linkage between ΔP and the superficial gas velocities at a temperature of 700 °C. (Used with permission from Ref. [109]. Copyright 2007, Elsevier).

This methodology provides valuable insights into the complex dynamic of fluidisation behaviour, which contributes to a thorough understanding of the system's performance at different gas velocities.

Fig. 13 depicts the experimental outcomes for increasing gas velocities, revealing a distinctive curve usually associated with catalyst particles having a broad range of sizes. The research concluded that initially, partial fluidisation was obtained, as indicated by an intermediate pressure drop. This implied that larger particles have not yet achieved full fluidisation. As the gas velocity increased further, the system eventually approached a point where ΔP neared W/S (W is the mass of carbon product (kg); S is the cross-sectional area (m^2)), suggesting that full fluidisation was achieved and would remain constant until the gas reached terminal velocity [109]. According to the study's findings, $U_{mf\text{-}pb}$ corresponds to the partial fluidisation of nitrogen gas at 0.47 cm (STP)/s. Full fluidisation was determined by observing $U_{mf\text{-}eb}$ at 0.72 cm (STP)/s, suggesting a constant pressure drop was maintained, confirming the state of complete fluidisation. During the process of CMD, the agglomeration of filamentous carbon on the fresh catalyst particle disrupts its fluid dynamic behaviour. This is due to the deposited carbon materials increasing particle diameter and decreasing density. Consequently, both the power of fluidisation and catalytic activity are compromised, resulting in the diminishing of hydrogen yield and CMD efficiency. Two distinct catalyst types were used, allowing for a comparison analysis to determine the superior catalyst.

Moreover, Amin et al. [106] reported that when the superficial velocity surpassed U_{mf}, the methane conversion rate observed for $Ni/\gamma Al_2O_3$ and Ni/SiO_2 was decreased. This was attributed to the accelerated formation of bubbles in terms of number and size at higher flow rates, negatively impacting the efficiency of reactant gas interaction with catalyst particles. Beyond U_{mf}, the flow rate tends to encounter mass transfer limitations because a bubbling regime influences the conversion rate [113,115]. However, Amin et al. [106] made an interesting observation: after 3 h from the commencement of the reaction, increased flow rates exhibited a similar deactivation pattern collected from Pinilla et al. [109,127] data set. This suggests that the deactivation pattern is more influenced by the blockage of catalyst active sites from carbon encapsulation rather than the bubble formation.

4.2.2. Experimental examples utilising U_{mf}

Various research articles were examined to assess the validation of the methodology introduced by Pinilla et al. [109,127]:

Quian et al. [110] investigated CMD using a 40 wt% Fe/Al_2O_3 catalyst in a fluidised bed reactor and compared the findings with a fixed-bed reactor. Optimising the fluidised-bed reactor necessitated understanding U_{mf}, a critical parameter. Therefore, Quian et al. [110] adopted the approach of Pinilla et al. [109,127] by linking pressure drop and velocity for 40 wt% Fe/Al_2O_3, examining two distinct bed heights of 0.4 and 2 cm. Fig. 14 illustrates U_{mf} measurements in two different bed sizes (0.4 and 2 cm) using inert nitrogen, explicitly chosen to mitigate the agglomeration issue observed with methane. The 0.4 cm bed showed no pressure drop (depicted by the blue line in Fig. 14) owing to the gas bypass, while the 2 cm bed showed partial fluidisation at a nitrogen gas velocity of 24.71 mm/s (V_{mf}), which corresponds to P_{mf} of roughly 3.22 mbar. As the gas flow rate was raised further to 30.06 mm/s, the pressure drop decreased somewhat, and the entire bed was fluidised. The pressure drop (P_{max} = W/A) remained constant and did not vary with increasing gas velocity until 45.34 mm/s. Lastly, similar to Pinilla et al. [109,127], the nitrogen velocity was corrected by a factor of 1.4 to account for methane.

In addition, Torres et al. [117] delved into the effects of methane conversion using Fe/Al_2O_3 catalysts at space velocities – 3, 6, and 8 $L_N/(g_{cat}.h)$ – while maintaining a constant temperature of 800 °C. The velocity at 3 $L_N/(g_{cat}.h)$ was below U_{mf}, featuring a fixed-bed characteristic. Fig. 15 depicts an enhancement in hydrogen yield rate when the space velocity was reduced from 8 to 3 $L_N/(g_{cat}.h)$. All the velocity curves had a persistent trend, implying a progressive decline in methane

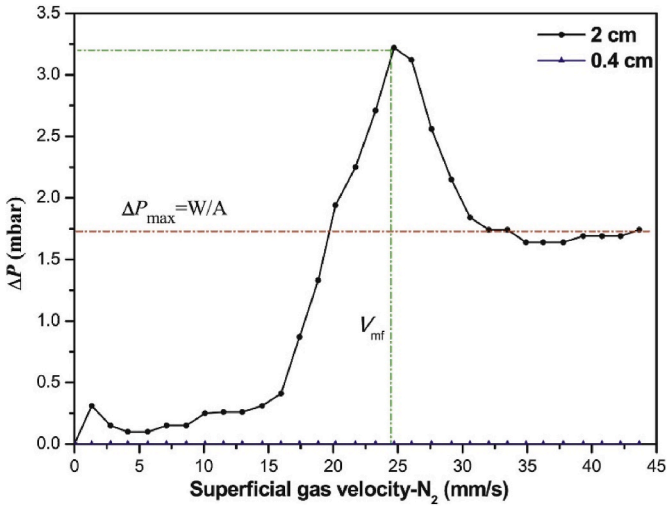

Fig. 14. U_{mf} measurements in two distinct bed sizes (0.4 and 2 cm) using inert nitrogen and a temperature of 750 °C. (Used with permission from Ref. [110]. Copyright 2019, Elsevier).

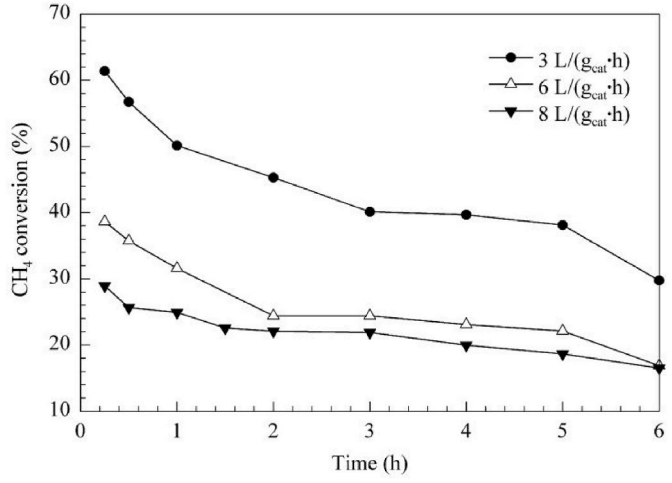

Fig. 15. A correlation between methane conversion (%) and time (h), where the space velocities are altered between 3, 6, and 8 $L_N/(g_{cat}.h)$. (Used with permission from Ref. [117]. Copyright 2012, Elsevier).

conversion, indicating continuous catalyst deactivation. As a result, it is proven that space velocity is a critical parameter in bed fluidisation. From Section 3, when compared to fixed bed reactors, fluidised beds provide better mixing conditions that allow exposure of all catalyst particles to methane gas, resulting in higher yields. However, as shown in Fig. 15, a significant rise in space velocity exceeding U_{mf} has a detrimental effect on catalyst bed behaviour. This deviation from optimal fluidisation is due to excessive bubble formation leading to inadequate catalyst-gas interaction, thus corroborating with Amin et al. [106] study.

4.3. Effect of particle size

According to a model proposed by Bi et al. [129], an increase in particle size and density will elevate U_{mf}. Hence, this section will delve into particle characterisation and clarify how particle size and density are important parameters to consider when operating an efficient fluidised-bed reactor. Geldart (1973) classified fluidisable particles into four groups depending on their properties at ambient conditions: A, B, C, and D (see Table 6 for explanation) [122,130].

Table 6
Classification of powders into Geldart Groups A, B, C, and D based on their fluidisation behaviour, with a description for each group.

Particle Group	Description
Group A Particles:	These particles have a small mean size (20–100 μm) and low particle density (<1.4 g/cm^3). Under ambient conditions and at U_{mf}, a non-bubbling fluidisation regime is initiated. Subsequently, as the flow rate increases, the bed undergoes significant expansion, followed by minimum bubbling fluidisation (U_{mb}) when velocity surpasses U_{mf} [123,130,131].
Group B Particles:	These particles exhibit a mean size and dense density ranging between 40 and 500 μm and 1.4 g/cm^3 – 4 g/cm^3, respectively [131]. As opposed to Group A, little to no bed expansion was noticed. Only at or slightly above U_{mf} does bubbling fluidisation occur ($U_{mf} = U_{mb}$).
Group C Particles:	These particles have characteristics of being very fine and cohesive [131]. In this scenario, achieving normal fluidisation is tremendously difficult due to fine particles having stronger London-van der Waals (cohesive forces) that form stable conglomerates. These forces are more substantial in comparison to the drag and buoyancy force exerted by the fluid onto the particles [113,131].
Group D Particles:	These particles are large and/or excessively dense. Therefore, their fluidisable capability is poor, leading to the formation of deep spouting beds as a substitute [123,130]. Similar to Group B, there is little bed expansion, resulting in ($U_{mf} = U_{mb}$).

In essence, from various literature and experimental reports on methane conversion, due to Group A powders having excellent fluidity and high mass transfer efficiency, most catalytic particles for catalytic cracking fall within this category in terms of mean size and density [19,59,125,132–137]. Therefore, selecting Geldart A catalytic particles is pivotal for achieving smooth fluidisation and successful methane conversion. This option ultimately ensures superior gas-solid contacting efficiency, wherein bubbles at U_{mb} continuously divide and coalesce until the maximum stable bubble size is attained [123,134]. On the other hand, when compared to particles within Groups B and D, where $U_{mf} = U_{mb}$, bubbles expand without reaching their full size, leading to significant pressure fluctuations and poor fluidisation quality [130]. However, with this in mind, various reports investigate a range of operating conditions and predominately focus on utilising either Geldart Type A or B particles to optimise fluidisation. Some experimental reports delve into the application of Geldart B particles, particularly concerning CMD [138–140]. Additionally, the bubbling fluidisation regime in a gas-fluidised system is the most prevalent in various industrial sectors such as methane cracking, olefin production and manufacturing of carbon nanotubes (CNT); therefore, this will be further explained in Section 5.1 [123].

However, the fluidisation quality can vary depending on the specific reaction and elevated temperatures. According to Geldart's classification, the fluidisation behaviour of powders under different groups can easily be anticipated under ambient conditions. Yet, researchers must consider that during CMD at temperatures exceeding 500 °C, the fluidisation properties of the catalytic particles may differ significantly from those at ambient temperature [125]. This discrepancy is a consequence of how gas properties influence Geldart catalytic grouping, potentially having a significant impact on fluidised bed operations. Furthermore, alteration in bed conditions, driven by factors like "elutriation of fines; attrition; agglomeration of particles; bed solid characteristics change due to reaction; density and viscosity of fluids alteration due to reaction and temperature", can considerably impact U_{mf} [125]. Therefore, catalytic particles may fall under different Geldart group types at conditions that significantly deviate from the ambient state.

4.3.1. Experimental studies involving particle characterisation

As previously emphasised, Geldart A particles are usually preferred when the objective is to achieve smooth and extensively expanded fluidisation. However, only a few researchers have explored comparing

diverse catalytic particle sizes across different characterisation groups under the same reaction conditions. Among these selected researchers, Lee et al. [134] conducted an in-depth study evaluating various particle sizes of activated carbon that belonged to different Geldart Group. The intention was to find the optimum particle size required to enhance the operation of a fluidised bed reactor. A fixed reaction temperature of 850 °C was utilised, while the particle size varied from 49.5 to 300 μm. As seen in Fig. 16, a clear trend was distinguished, where smaller particles exhibited a higher methane conversion rate. This phenomenon is attributed to smaller particles' larger surface area-to-particle volume ratio, allowing for more effective mass transfer. However, the influence of particle size on CMD is diminished as the reaction advances over time, refer to Fig. 16.

Additionally, the particle size of 108 μm consistently demonstrated the most favourable and stable during CMD. This particle size falls within the Geldart A particle characterisation range, as detailed in Section 4.3. As a result, the combination of increased surface area and the superior fluidisation quality from 108 μm activated carbon particles ultimately led to a higher methane conversion within the fluidised bed reactor.

Additionally, as previously stated, the U_{mf} is experimentally quantified by analysing pressure drop as a function of gas velocity. This measure is dependent on factors like particle size, density, Geldart Group classification, and fluid characteristics [125]. Therefore, this link has allowed researchers to compare different catalyst types by altering the superficial velocity. In ambient conditions, Li et al. [133] initially explored fluidisation behaviour using pure Ni/Al_2O_3 (particle size 10–100 μm) and Ni/Al_2O_3 mixed with Al_2O_3 particles. Data collected for pure Ni/Al_2O_3 (Fig. 17a) and Ni/Al_2O_3 mixed with Al_2O_3 (Fig. 17b) concluded that increasing superficial velocity led to catalytic particles undergoing stages of "slugging, channelling, disrupting and agglomerating fluidisation". Fig. 17a establishes that as the superficial velocity surpasses U_{mf}, the pressure drop would remain constant at 46 Pa, significantly below the theoretical bed pressure drop of 65 Pa. This suggests poor fluidisation quality attributed to cohesive catalyst particles agglomerating, a characteristic often associated with Geldart Group C particles. Therefore, Li et al. [133] enhanced the fluidisation quality by thoroughly mixing Al_2O_3 with Ni/Al_2O_3 catalyst to introduce

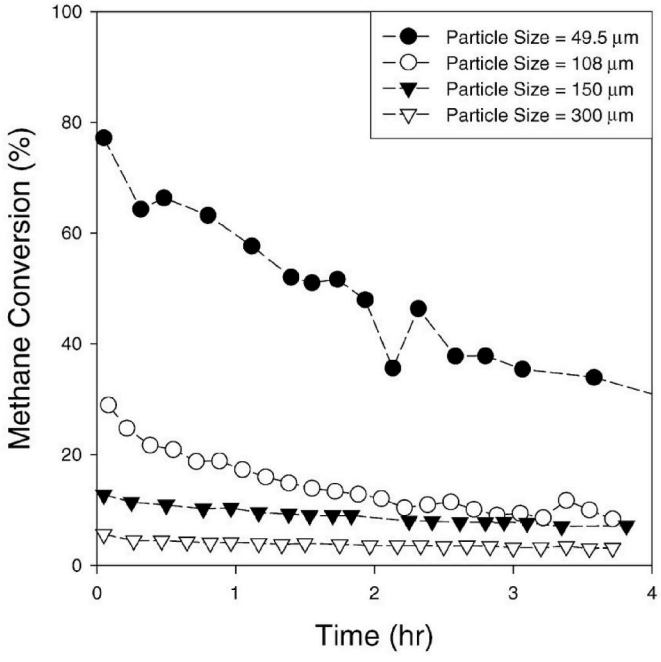

Fig. 16. Effect on methane conversion (%) when the AC catalytic particle size is altered. (Used with permission from Ref. [134]. Copyright 2004, Elsevier).

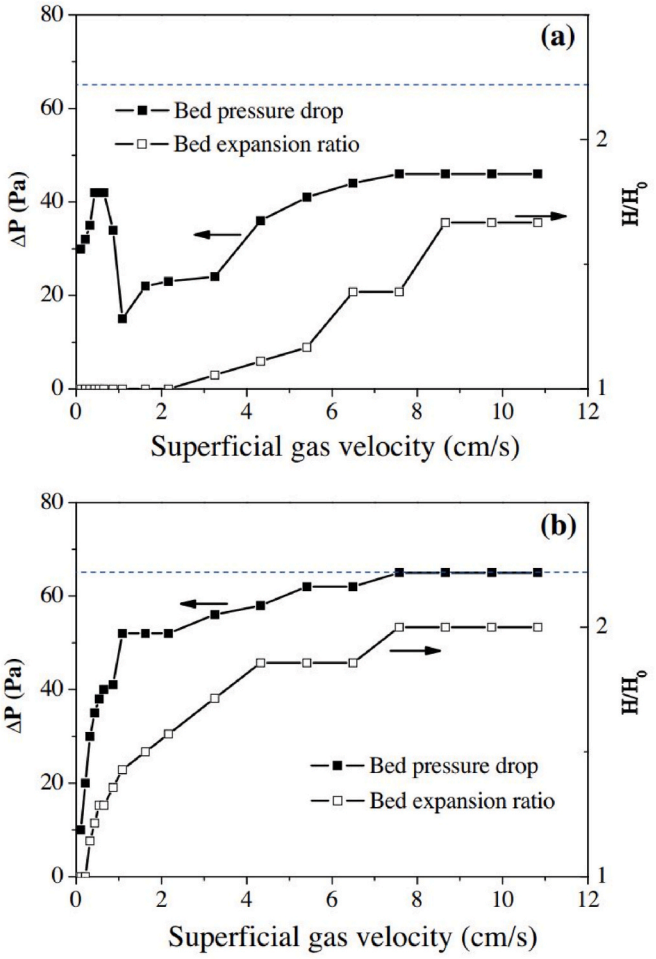

Fig. 17. Bed pressure drop curves of (a) pure Ni/Al_2O_3 and (b) Ni/Al_2O_3 mixed with Al_2O_3. (Used with permission from Ref. [133]. Copyright 2013, Elsevier).

particles of different sizes, where the cohesive problem was solved. As depicted in Fig. 17b, the bed pressure drop corresponded with the theoretical value and surpassed that of the pure Ni/Al_2O_3. These findings highlight that adding Al_2O_3 particles significantly enhances the fluidisation quality by expanding the fluidisation, resulting in a high gas dispersion coefficient [141].

In experimental research, Group B catalytic particles are frequently used to investigate fluidisation behaviour, as they include features that transition the fluidisation characteristic from Group A to Group C [141]. Usually, as the reaction is processed in CMD, the U_{mf} particle size and density would vary drastically due to carbon encapsulation, particle agglomeration, and attrition. These phenomena were emphasised in work done by Hadian et al. [140], who used 56 wt% of Ni on silica support to conduct thermocatalytic methane cracking. Their research sought to comprehend the catalyst's performance throughout the reaction's lifecycle. The catalyst's particles were initially categorised as B-type in their fresh condition but changed to D-type when their activity diminished. Catalyst characterization included measuring parameters such as BET surface area and pore volume with a Thermo Fisher Scientific Analyzer (as discussed in Section 3.3). The findings demonstrated a considerable decline in specific surface area and pore volume, suggesting that limited catalyst pores were occupied by carbon. This resulted in an increase in particle size and a significant 32% decrease in bulk density of the catalyst particle, attributed to carbon layering on the catalyst.

Moreover, Parmar et al. [139] recently aimed to investigate the CMD in a bubbling fluidised-bed reactor to produce blue hydrogen and CNT.

Group B catalytic particles are often found when a bubbling fluidised bed is being employed due to the characteristic of having $U_{mf} = U_{mb}$. They utilised a catalytic composition of (60%Ni–5%Cu–5%Zn/Al_2O_3) characterised as Group B, with an average particle size and density of 125 μm and 1.1 g/cm^3, respectively. Bubbling fluidisation was achieved at a superficial velocity of 1.8U_{mf}; however, over time, the catalytic activity was eventually diminished, with reasons similar to what was observed by Hadian et al. [140].

5. Fluidisation regimes

Muradov et al. [59] highlighted that when the gas velocity increases, the system is likely to go through numerous regimes, including: "the bubbling regime, the slugging regime (occurs only in the reactors with small diameters), the turbulent regime, fast fluidisation and pneumatic transport" (see Fig. 18 for visualisation). Zhou et al. [142] portrayed gas-solid systems at different stages, where the movement of catalytic particles becomes more vigorous as the superficial velocity increases beyond U_{mf} and U_{mb}. This section will further explore the relevant fluidisation regimes beyond the U_{mb} point that complement CMD.

5.1. Bubbling regime

As the gas velocity increases and surpasses the U_{mb}, gas bubbles begin to form [113]. Generally, the majority of gas-fluidised beds run on a bubbling regime [123]. Toomey and Johnstone's (1952) [130] two-phase fluidisation hypothesis notation provides a fundamental insight into how a bubbling fluidised bed expands. This concept describes the two distinct modes that make up the bubbling fluidised bed-the lean/ bubble phase (the gas bubbles), which is characterised by the rising gas bubbles detached from the continuous bed particles, and the dense/emulsion phase, which is characterised as the bed particles fluidised by the high flow-rate gas [113,130]. Additionally, Yasui (1958) et al. [143] were among the first to explore the characteristics of bubble formation by employing two fluidised bed reactors and gathering experimental data using light-transmitting probes.

When visualising a bubbling bed (see Fig. 19), the solid catalytic particles accumulate in the dense continuous phase, establishing direct contact with the methane gas. However, the bubble phase transports both the gas and catalyst particles through a discontinuous phase, where the particle generates a dense phase that is raised within the spherical bubble-referred to as the wake volume (see Fig. 19) [123,144]. The characteristics of the bed particles, especially their size, influence the form of the bubbles; generally, the smaller the particles, the greater the ratio of wake volume to bubble volume [123]. Therefore, particles from Group A (refer to Section 4.3 Powder Classification) are classified as optimum when it comes to bubble fluidisation.

Additionally, the hydrodynamics and efficiency of bubbling fluidised-bed reactors are significantly influenced by several crucial parameters, among which bubble size holds great importance. Over the years, numerous academic studies have been conducted to examine the coalescence of bubbles in a gas-solid fluidised bed reactor [145–151]. In an active fluidised bed reactor, bubbles are observed to coalesce and split simultaneously when rising from the distributor [123]. Therefore, the bubble diameter measurement must be a balance between the bubble coalescence and splitting, a state commonly referred to as an equilibrium bubble size [123,152]. Darton et al. [153] had initially observed that as the bubbles ascend through the system, their sizes tend to increase. In particular, Geldart Group A particles can reach and achieve their equilibrium bubble size within a small reactor rig. However, Geldart Group B particles are limited in their ability to attain equilibrium size in a laboratory-scaled reactor, necessitating the addition of a higher bed height commonly associated with industrial-scale application (refer to Fig. 19).

Nevertheless, both Knowlton [154] and Seville et al. [123] have indicated that upscaling a bubbling bed reactor may lead to gas bypassing through the system. Gas bypassing will only be susceptible when operating a large bubbling bed using Group A type particles, which can disrupt the gas-solid interactions. This scenario arises due to the pressure difference, where the pressure at the bottom of the reactor would be higher compared to the top. As a result, gas compression occurs, inhibiting fluidisation to commence.

5.1.1. Experimental studies involving bubbling-fluidised bed reactor

Almost every feature of fluidised bed reactors, including gas and particle residence periods, particle entrainment and elutriation, heat and mass transport, and reaction conversion, is greatly influenced by bubble characteristics such as size, shape, and velocity [137]. As a result, when examining a bubble-fluidised bed reactor, most reports devote their analysis to bubble characterisation. However, this section will briefly touch upon some of the current experimental studies that have already used bubbling fluidised bed reactors to catalytically decompose methane into hydrogen:

Keller et al. [136] generated porous and fluidisable catalysts using spray-drying of 10 wt-% Fe_2O_3 and 90 wt-% Al_2O_3. A laboratory-scale fluidised bed reactor was utilised, where the gas flow rate was carefully chosen, allowing vigorous mixing and obtaining characteristics of a bubbling bed. A series of 14 experiments were conducted using this reactor bed configuration, which had operating parameters including a minimum temperature of 750 °C, gas velocity exceeding U_{mf} of 0.28 cm/s and a reaction run time of 90 min. The objective of this study was to collect kinetic data that could be incorporated into the design and

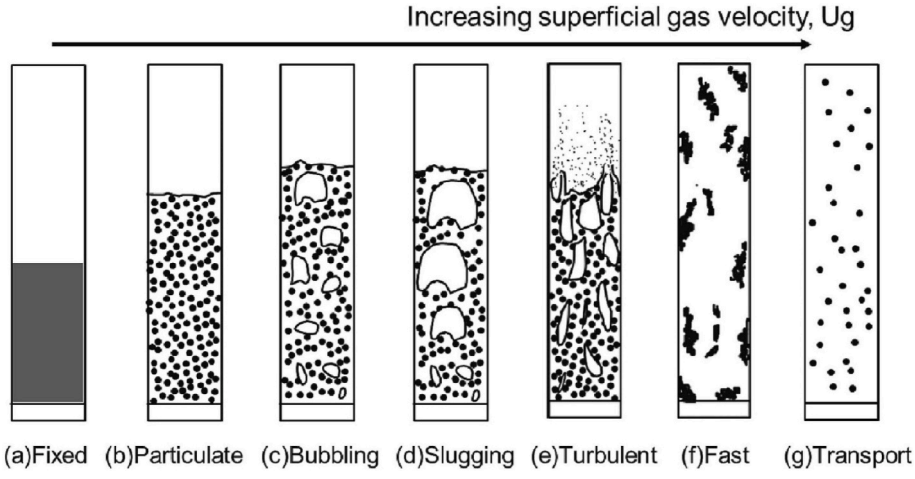

Fig. 18. Flow pattern of various regimes as the superficial velocity increases. (Used with permission from Ref. [142]. Copyright 2013, Elsevier).

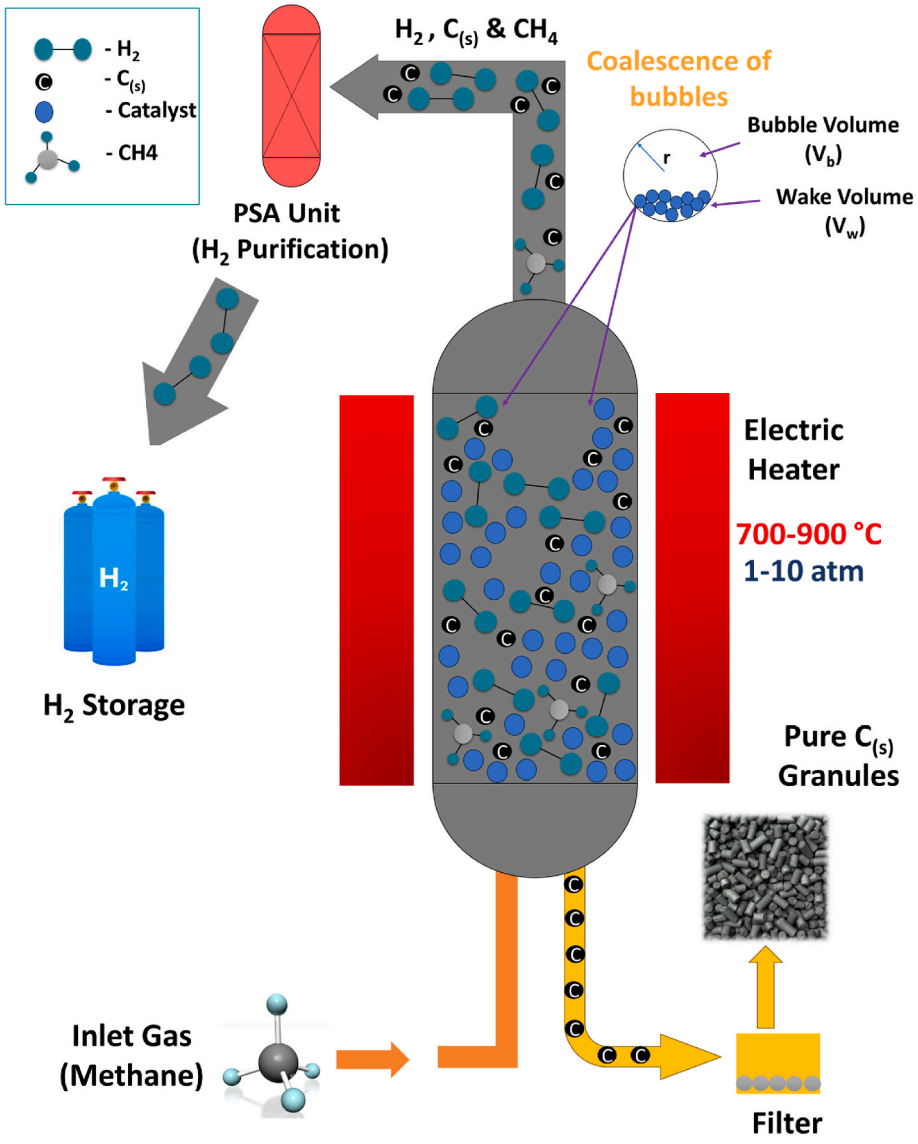

Fig. 19. A typical bubbling fluidised-bed reactor used from an industrial standpoint. (For a more precise understanding, please refer to the key in the top left corner, which highlights the components represented in the figure).

scaling-up of the CMD process.

Ammendola et al. [138] conducted CMD experiments using copper catalysts with γ-alumina support operating under a laboratory-scale bubbling fluidised bed reactor. Their investigation encompassed a wide range of variables, including the total flow rate, catalyst quantity (contact time), reaction temperature, and CH_4 intake concentration. This comprehensive report aimed to generate data detailing the conversion of CH_4 to H_2, the deposition of carbon on the catalyst, and the deactivation time. Furthermore, the U_{mf} was experimentally determined by analysing the pressure drop curve against the superficial velocity with a temperature range of 700–800 °C. The obtained gas velocity was in conjunction with the Wen et al. [155] literature correlation, explaining that the reactor bed certainly operated under a bubbling fluidisation regime.

Subsequently, Ammendola et al. [156] later developed a model to consider the behaviour of an individual catalytic particle when undergoing each step of methane decomposition within a bubbling fluidised-bed reactor. This model offered insights into the reaction process in the reactor, hence allowing the optimisation of the bubbling-bed reactor. Ammendola et al. [156] acknowledged the two-phase theory, explained further in Section 5.1. Further analysis of mass transfer between the dense and bubble phases was explored, concluding that particle diffusion between the bubble and the dense phase led to relatively constant bubble size. However, bubble size and volume variations were still noticed, explaining that bubbles are prone to coalescence, resulting in the variation of size, and the methane conversion along the bed axis led to changes in volume. Remarkably, a strong correlation between the model and experimental methane conversion from the start to the deactivation step was observed, proving the significance of the model.

Similarly, in a parallel study, Muradov et al. [59] developed a mathematical model for predicting the reaction performance in a bubbling fluidised bed reactor. This study shares many similarities with the work of Ammendola et al. [156]. However, a noticeable difference was observed in Muradov et al. [59] reports when describing a bubbling fluidised bed, which involves having three phases: the bubble phase, the wake phase and the dense phase-a modification from the earlier discussed two-phase model. Additionally, for bubbling fluidised beds, a countercurrent back-mixing model with solids circulation was also implemented. The comparison between the experimental data and the model predictions for methane conversion concerning expanded bed height is illustrated in Fig. 20. The experimental set-up employed a

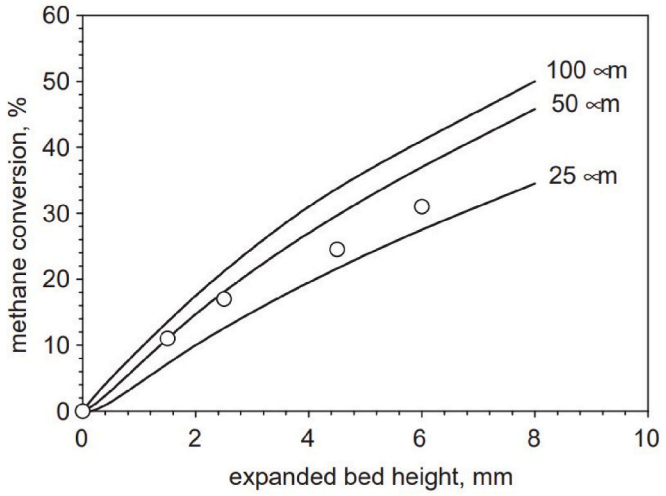

Fig. 20. The contrast between experimental data and model projections for methane conversion using AC at particle sizes of 25, 50 and 100 μm (Used with permission from Ref. [59]. Copyright 2005, Elsevier).

small-scale fluidised bed reactor with activated carbon particles (size averaging 50-100 μm) under a bubbling flow regime. On the other hand, the modelling considered carbon particles of varying sizes: 25 μm, 50 μm, and 100 μm. The comparison shows a generally acceptable correspondence between model predictions and experimental findings, which is especially clear for smaller expanded bed heights.

Therefore, considering the accuracy of the mathematical modelling derived from both Muradov et al. [59] and Ammendola et al. [156], there is a compelling indication that the upscaling of a bubbling fluidised bed could be pursued, employing larger geometric diameters that align with established industrial standards. Nonetheless, scaling up still poses challenges, as the prediction of U_{mb} can be very challenging when the reactor's geometry is altered significantly. As noted by Pinilla et al. [127], an excessively high U_{mb} can lead to the enlargement of bubbles within the fluidised bed reactor, causing the gas to pass through the particle bed without efficient contact with the catalyst particles. Pinilla et al. [127] found the optimum U_{mb} for the appropriate catalytic particle by running empirical, experimental studies, where eventually, the smallest increase in pressure drop during CMD was found, illustrating smooth fluidisation. However, conducting multiple large-scale runs can prove costly, making this approach less appealing. Additionally, Chew et al. [157] noted that being heavily reliant on laboratory-scale observation may result in missed insight, as at a smaller scale, the occurrence of slugging behaviour could potentially lead to inaccurate conclusions. Therefore, factoring in scale-up requirements early on can have the significant advantage of minimising the time and financial investments needed for successful process scale-up.

5.2. Turbulent regime

Turbulent fluidised bed behaviour is commonly defined by rapid and chaotic small-scale movements, where transient voids flow diagonally upward within the column [158]. Pressure fluctuations, unlike those in bubbling and slugging beds, are smaller in magnitude and possess higher frequencies. The initiation of turbulent fluidisation is believed to occur when bubbles or slugs swiftly disintegrate with a slight rise in gas flow rate. The disintegration commences when the superficial gas velocity surpasses U_{mb}; bubbles expand beyond their maximum size and become unstable, resulting in a prevalence of bubble splitting, which is the dominant component over bubble coalescence [113].

As discussed in Section 5.1, it is already evident that bubbling fluidised-bed reactors are dominating the experimental field for CMD. However, as highlighted by Chew et al. [157], turbulent fluidised-bed reactors are more likely to be employed on an industrial scale. The chaotic mixing of particles and gas allows for an enhanced heat and mass transfer as opposed to a bubbling fluidised bed reactor [159]. Chew et al. [157] conducted a comparative analysis of first-order reaction conversion across various fluidisation regimes (see Fig. 21). It is apparent that the bubbling bed reactor only achieved a conversion of approximately 30%, while the turbulent fluidised bed reactor reached an impressive conversion rate of over 80%. This again validates the superior mass transfer capabilities of the turbulent regime in contrast to the bubbling regime.

5.2.1. Experimental studies involving turbulent fluidised bed reactor

As previously discussed, a turbulent fluidised bed reactor offers distinct advantages over bubbling bed reactors on a commercial scale for CMD. However, there is limited literature that specifically addresses experimental studies regarding turbulent bed reactors and hydrogen production through CMD. So far, researchers have thoroughly examined and recognised the bubbling, slugging and fast fluidisation flow pattern, while the turbulent fluidisation flow pattern has not been widely recognised as a unique flow regime [160]. It is noteworthy that some researchers have explored the application of turbulent fluidised bed reactors for CNT production [161–168]. Interestingly, CNT production involves the requirement of converting methane to produce high-purity CNT and hydrogen by-products.

Yun et al. [162] introduced an innovative approach by integrating a Downer reactor with a turbulent fluidised bed reactor for synthesising single-walled carbon nanotubes (SWCNTs) from CH_4 using a Fe/MgO catalyst. This coupling of the two reactors improved both the selectivity and yield of SWCNTs. Notably, enhancing the yield of SWCNTs will subsequently elevate the production of hydrogen (the required product), as per Equation (4). In this two-stage process, methane was initially mixed with the catalytic particles in the Downer reactor, where the catalyst underwent reduction by methane gas at a temperature of 900 °C. The resulting mixture containing the used catalyst, SWCNTs and gases was subsequently directed into the turbulent fluidised bed reactor, which was also maintained at 900 °C. Here, a fresh gas feed was also introduced into the system at a gas velocity of 0.3 m/s, and with a catalyst residence time of 3–6 min, a sufficient quantity of SWCNTs was collected. The influence of the catalyst and the size distribution of SWCNTs were investigated using various techniques such as Raman spectroscopy, TGA, and TEM. The findings indicated that the coupling of the turbulent fluidised bed reactor had increased the production of SWCNTs by 50 folds, suggesting the potential of upscaling this technology and, therefore, enhancing the synthesis of both SWCNTs and hydrogen.

Hao et al. [165] conducted an experimental study on generating agglomerated CNT through propylene pyrolysis, utilising a $Fe/Mo/Al_2O_3$ catalyst. A turbulent regime was achieved in the fluidised bed reactor when the gas flow rate surpassed 0.05 m/s. This specific flow rate of propylene, diluted with nitrogen, was carefully controlled to ensure the attainment of turbulent conditions at the reaction temperatures of 923 K. Hao et al. [165] have specifically highlighted the favourable transfer characteristic inherent in turbulent fluidisation, therefore, to obtain high selectivity and yield of CNT production, the reaction conditions were carefully maintained. Similarly, Wei et al. [164] also investigated the formation of CNT agglomerates and the mass production of CNT. Their approach was similar to that of Hao et al. [165], as here propylene decomposition was again conducted using $Fe/Mo/Al_2O_3$ catalyst to mass produce CNT materials. The insightful data gathered concludes that the turbulent regime displayed a highly expanded and smooth fluidisation behaviour.

If the application of turbulent bed reactors proves to be a success when undergoing propylene pyrolysis to produce CNT experimentally, then implementing/ retrofitting this regime behaviour towards hydrogen production could be further explored. This approach could involve further investigation and optimisation of the reactor behaviour,

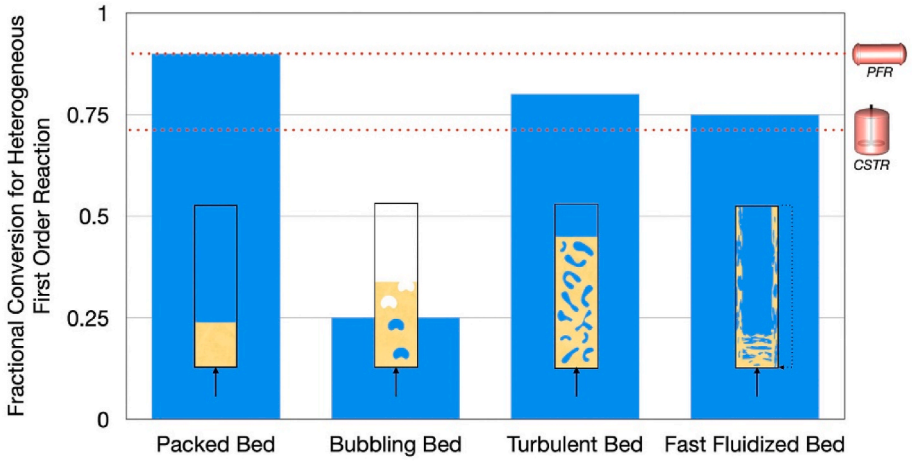

Fig. 21. Displays first-order reactions with various fluidisation regimes. (Used with permission from Ref. [157]. Copyright 2022, Elsevier).

with the goal of eventually achieving successful upscaling of the reactor for commercial use. Muradov et al. [59] have already developed a mathematical model that explored and simulated the reactor performance of a turbulent fluidised bed reactor when undergoing CMD. In this particular study, the carbon flow rate was calculated using a methane conversion rate of 38%, which corresponds to the highest achieved conversion rate seen in lab-scale tests using activated carbon. Importantly, the outcome of the model prediction was comparable with the actual experimental outcome. Therefore, future research could involve using this already established model as a foundation for analysing and comparing experimental data gathered using a turbulent fluidised bed.

6. Future perspective and conclusion

Methane cracking technology is not commercially available due to its lack of economic viability compared to SMR technology. Nevertheless, methane cracking has gained much interest from both panels of scientists and government agencies as optimising its efficiency and durability could lead to low to near-zero CO_2 emissions on an industrial scale. It has been emphasised that fixed-bed reactors are the most common and basic configurations used for performing CMD in laboratory-based settings. Thus far, characterisation methods such as SEM, TEM, XRD, BET, and TGA have proven essential for understanding catalyst behaviour and the deactivation phenomena. A comprehensive analysis revealed that most experimental literature utilises multiple characterisation techniques to gain complementary insights into various aspects of catalyst morphologies, composition and surface properties upon deactivation. Furthermore, fluidised bed reactors are more suitable for industrial-scale applications when interpreting CMD. Consequently, extensive analysis has been conducted to understand the fluidisation characteristics, which focuses on the optimisation of temperature, superficial gas velocity, and particle size/density. Upon investigating various experimental reports, techniques for optimising each parameter were distinguished, thereby enabling efficient operation of the fluidised bed furnace. However, scaling up fluidised bed reactors remains challenging due to mass transfer limitations.

Finally, different fluidisation regimes were interpreted, with the bubbling regime appearing more promising for upscaling a fluidised bed reactor from both an experimental and modelling perspective. However, there is a lack of experimental studies that highlight using turbulent fluidised bed reactors when achieving high hydrogen yield from CMD. Although some studies have explored pyrolysis reactions in the context of CNT production, it is reasonable to assume that since CNT production has reached a commercial level, there is potential for utilising turbulent fluidised beds. Nevertheless, the scarcity of experimental studies investigating CMD using turbulent fluidised bed reactors can be attributed to their non-commercial availability. Therefore, future efforts could focus on incorporating turbulent fluidised bed reactors into experimental studies. The data from such studies could then be used to extrapolate and compare with industrial-scale reactors.

Industrial manufacturing of CNT is the closest and most similar technique to conventional methane cracking; thus, integrating these technologies is highly plausible and may prove successful. However, substantial expenses are incurred when experimentally testing the various CNT methodologies on methane cracking. Therefore, it is advisable to propose a computational fluid dynamic (CFD) simulation tool to design an optimally performing reactor using pre-existing technologies. The hydrodynamics of fluidised bed reactors are known to be highly complex, necessitating an empirical design process. CFD software can enhance the reactor efficiency by optimising bed parameters, temperature, gas superficial velocity and particle characteristics. Nonetheless, CFD simulations pose a challenge due to the requirement of experimental data for validation, which increases the overall cost.

Funding

This research was partially funded and supported by the Engineering and Physical Sciences Research Council (EPSRC), Loughborough University via EPSRC Centre for Doctoral Training in Sustainable Hydrogen - SusHy (EP/S023909/1) and the Doctoral College.

CRediT authorship contribution statement

Aryamman Sanyal: Writing – review & editing, Writing – original draft. **Weeratunge Malalasekera:** Writing – review & editing. **Hemaka Bandulasena:** Writing – review & editing. **K.G.U. Wijayantha:** Writing – review & editing.

Declaration of competing interest

The authors declare that they have no known competing financial interests or personal relationships that could have appeared to influence the work reported in this paper

Acknowledgements

Special thanks go to the academic staff of the Department of Chemistry, Mechanical Engineering and Chemical Engineering at Loughborough University for their support and assistance throughout this review. The author is also grateful for the funding that was provided by the EPSRC and the Doctoral College through the Centre for Doctoral

Training in Sustainable Hydrogen.

Appendix A. Supplementary data

Supplementary data to this article can be found online at https://doi.org/10.1016/j.ijhydene.2024.05.397.

References

[1] Rogelj J, Schaeffer M, Meinshausen M, Knutti R, Alcamo J, Riahi K, Hare W. Environ Res Lett 2015;10:105007–18.
[2] Home – Climate Change. Vital signs of the planet. https://climate.nasa.gov/. [Accessed 7 October 2022].
[3] Khashimwo P. J Asian Afr Stud 2021;56:1503–20.
[4] Rogelj J, Schleussner CF, Hare W. Geophys Res Lett 2017;44:10662–5.
[5] Voldsund M, Jordal K, Anantharaman R. Int J Hydrogen Energy 2016;41:4969–92.
[6] Zapantis A. Hydrogen production with CCS and bioenergy, vol. 2; 2019. p. 1–49.
[7] Government H. UK hydrogen strategy, vol. 3; 2021. p. 14–5.
[8] Ashik UPM, Wan Daud WMA, Abbas HF. Renew Sustain Energy Rev 2015;44:221–56.
[9] Hydrogen not the magical answer to zero-carbon prayers | Financial Times, https://www.ft.com/content/2b0db0aa-4b17-11ea-95a0-43d18ec715f5, (accessed 5 October 2022)..
[10] Ho MT, Wiley DE. In: Feron PHM, editor. Absorption-based post-combustion capture of carbon dioxide. first ed. Woodhead Publishing; 2016. p. 711–56.
[11] Faheem HH, Tanveer HU, Abbas SZ, Maqbool F. Fuel 2021;297. Article 120769.
[12] Pinilla JL, Suelves I, Lázaro MJ, Moliner R. J Power Sources 2009;192:100–6.
[13] Kalamaras CM, Efstathiou AM, Al-Assaf Y, Poullikkas A. Conference papers in energy, vol. 2013. Hindawi Publishing Corporation; 2013. p. 2–8.
[14] Lee CH, Mun S, Lee KB. J Power Sources 2015;281:158–63.
[15] Al-Qahtani A, Parkinson B, Hellgardt K, Shah N, Guillen-Gosalbez G. Appl Energy 2021;281:115958.
[16] Bhandari R, Trudewind CA, Zapp P. J Clean Prod 2014;85:151–63.
[17] Weger L, Abánades A, Butler T. Int J Hydrogen Energy 2017;42:720–31.
[18] Timmerberg S, Kaltschmitt M, Finkbeiner M. Energy Convers Manag X 2020;7:100043.
[19] Amin AM, Croiset E, Epling W. Int J Hydrogen Energy 2011;36:2904–35.
[20] Fan Z, Xiao W. Angew Chem 2021;133:7742–6.
[21] Sánchez-Bastardo N, Schlögl R, Ruland H. Chem Ing Tech 2020;92:1596–609.
[22] Sánchez-Bastardo N, Schlögl R, Ruland H. Ind Eng Chem Res 2021;60:11855–81.
[23] Samanta SK, Verma P. Sci Technol 2015;1:109–23.
[24] Serrano DP, Botas JA, Guil-Lopez R. Int J Hydrogen Energy 2009;34:4488–94.
[25] Abánades A, Rubbia C, Salmieri D. Energy 2012;46:359–63.
[26] Hasnan NSN, Timmiati SN, Lim KL, Yaakob Z, Kamaruddin NHN, Teh LP. Mater Renew Sustain Energy 2020;9:1–18.
[27] Borghei M, Karimzadeh R, Rashidi A, Izadi N. Int J Hydrogen Energy 2010;35:9479–88.
[28] Saraswat SK, Sinha B, Pant KK, Gupta RB. Ind Eng Chem Res 2016;55:11672–80.
[29] Kuvshinov GG, Mogilnykh YuI, Kuvshinov DG. Catal Today 1998;42:357–60.
[30] Hazra M, Croiset E, Hudgins RR, Silveston PL, Elkamel A. Can J Chem Eng 2009;87:99–105.
[31] Alstrup I, Tavares MT. J Catal 1992;135:147–55.
[32] Sharif Zein SH, Mohamed AR, Talpa Sai PS. Ind Eng Chem Res 2004;43:4864–70.
[33] Snoeck JW, Froment GF, Fowles M. J Catal 1997;169:250–62.
[34] Demicheli MC, Ponzi EN, Ferretti OA, Yeramian AA. Chem Eng J 1991;46:129–36.
[35] Zavarukhin SG, Kuvshinov GG. Appl Catal Gen 2004;272:219–27.
[36] Tong S, Miao B, Zhang L, Chan SH. Energies 2022;15:2573.
[37] Grabke HJ. Metall Trans A 1970;1:2972–5.
[38] Hamdan M, Halawy L, Abdel Karim Aramouni N, Ahmad MN, Zeaiter J. Fuel 2022;324:124455.
[39] Baker RTK. Carbon N Y 1989;27:315–23.
[40] Wei L, Tan YS, Han YZ, Zhao JT, Wu J, Zhang D. Fuel 2011;90:3473–9.
[41] Konieczny A, Mondal K, Wiltowski T, Dydo P. Int J Hydrogen Energy 2008;33:264–72.
[42] Pennycook SJ. In: Bassani F, Wyder P, Liedl GL, editors. Encyclopedia of condensed matter physics. first ed. Elsevier; 2005. p. 240–7.
[43] Yan W, Kent Hoekman S. Environ Prog Sustain Energy 2014;33:213–9.
[44] Younessi-Sinaki M, Matida EA, Hamdullahpur F. Int J Hydrogen Energy 2009;34:3710–6.
[45] Dixon AG, Partopour B. Annu Rev Chem Biomol Eng 2020;11:109–30.
[46] Tong S, Miao B, Chan SH. Chemical Engineering and Processing - Process Intensification 2023;186:109323.
[47] de Lima KPM, Dias V da F, da Silva JD. Int J Hydrogen Energy 2020;45:10353–69.
[48] Wehinger GD, Flaischlen S. Ind Eng Chem Res 2019;58:14410–23.
[49] Abbas SZ, Dupont V, Mahmud T. Int J Hydrogen Energy 2017;42:2889–903.
[50] Rout KR, Jakobsen HA. Can J Chem Eng 2015;93:1222–38.
[51] Herce C, Cortés C, Stendardo S. Fuel Process Technol 2019;186:137–48.
[52] Kuncharam BVR, Dixon AG. Fuel Process Technol 2020;200:106314.
[53] Lee H, Kim A, Lee B, Lim H. Energy Convers Manag 2020;213:112839.
[54] Karpilov I, Pashchenko D. Therm Sci Eng Prog 2023;42:101868.
[55] Worstell J. In: Adiabatic fixed-bed reactors. first ed. Butterworth-Heinemann; 2014. p. 35–65.
[56] Muradov N. Catal Commun 2001;2:89–94.
[57] Muradov N. Int J Hydrogen Energy 2001;26:1165–75.
[58] Muradov N. Int J Hydrogen Energy 2017;42:14058–88.
[59] Muradov N, Chen Z, Smith F. Int J Hydrogen Energy 2005;30:1149–58.
[60] Muradov N, Smith F, T-Raissi A. Catal Today 2005;102–103:225–33.
[61] Raval N, Maheshwari R, Kalyane D, Youngren-Ortiz SR, Chougule MB, Tekade RK. In: Tekade RK, editor. Basic fundamentals of drug delivery. first ed. Academic Press; 2019. p. 369–400.
[62] Omidi M, Fatehinya A, Farahani M, Akbari Z, Shahmoradi S, Yazdian F, Tahriri M, Moharamzadeh K, Tayebi L, Vashaee D. In: Tayebi L, Moharamzadeh K, editors. Biomaterials for oral and dental tissue Engineering. first ed. Woodhead Publishing; 2017. p. 97–115.
[63] Suelves I, Lázaro MJ, Moliner R, Corbella BM, Palacios JM. Int J Hydrogen Energy 2005;30:1555–67.
[64] Bayat N, Rezaei M, Meshkani F. Int J Hydrogen Energy 2016;41:1574–84.
[65] Yang L, Wu X, Liu F, Zhang X, He J, Saito K. Int J Hydrogen Energy 2020;45:13245–55.
[66] Suelves I, Lázaro MJ, Moliner R, Pinilla JL, Cubero H. Int J Hydrogen Energy 2007;32:3320–6.
[67] Moliner R, Suelves I, Lázaro MJ, Moreno O. Int J Hydrogen Energy 2005;30:293–300.
[68] Musamali R, Isa YM. Int J Energy Res 2018;42:4372–82.
[69] Ramasubramanian V, Ramsurn H, Price GL. Int J Hydrogen Energy 2020;45:12026–36.
[70] Tapia-Parada K, Valverde-Aguilar G, Mantilla A, Valenzuela MA, Hernańdez E. Fuel 2013;110:70–5.
[71] Harun K, Adhikari S, Jahromi H. RSC Adv 2020;10:40882–93.
[72] Tang L, Yamaguchi D, Burke N, Trimm D, Chiang K. Catal Commun 2010;11:1215–9.
[73] Raja PB, Munusamy KR, Perumal V, Ibrahim MNM. In: Iqbal HMN, Bilal M, Nguyen TA, editors. Nano-bioremediation: fundamentals and applications. first ed. Elsevier; 2022. p. 57–83.
[74] Inan TY. In: Visakh PM, Markovic G, Pasquini D, editors. Recent developments in polymer macro, micro and nano blends: preparation and characterisation. first ed. Woodhead Publishing; 2017. p. 17–56.
[75] Wang GC. In: The utilization of slag in civil infrastructure construction. first ed. Woodhead Publishing; 2016. p. 87–113.
[76] Murata K, Inaba M, Miki M, Yamaguchi T. React Kinet Catal Lett 2005;85(1):21–8. 2005, 85.
[77] Zhou L, Enakonda LR, Saih Y, Loptain S, Gary D, Del-Gallo P, Basset JM. ChemSusChem 2016;9:1243–8.
[78] Szymańska M, Malaika A, Rechnia P, Miklaszewska A, Kozłowski M. Catal Today 2015;249:94–102.
[79] Jaroniec M, Kruk M, Sayari A. Stud Surf Sci Catal 1998;117:325–32.
[80] Liu R, Meng Y, Gu D, Tu B, Zhao D. Stud Surf Sci Catal 2007;170:1721–33.
[81] Nasrollahzadeh M, Atarod M, Sajjadi M, Sajadi SM, Issaabadi Z. Interface Science and Technology 2019;28:199–322.
[82] Mahmoodzade E, Meshkani F, Rezaei M, Rastegarpanah A. J Energy Inst 2020;93:2488–96.
[83] Pinilla JL, Utrilla R, Karn RK, Suelves I, Lázaro MJ, Moliner R, García AB, Rouzaud JN. Int J Hydrogen Energy 2011;36:7832–43.
[84] Pudukudy M, Yaakob Z, Takriff MS. Appl Surf Sci 2015;356:1320–6.
[85] Pudukudy M, Yaakob Z, Jia Q, Takriff MS. Appl Surf Sci 2019;467–468:236–48.
[86] Liu F, Yang L, Song C. Int J Hydrogen Energy 2018;43:5501–11.
[87] Bai Z, Chen H, Li B, Li W. J Anal Appl Pyrolysis 2005;73:335–41.
[88] Guil-Lopez R, Botas JA, Fierro JLG, Serrano DP. Appl Catal Gen 2011;396:40–51.
[89] Liu F, Chen L, Yang L, Fan Z, Nikolic H, Richburg L, Liu K. Int J Hydrogen Energy 2016;41:4592–602.
[90] Ahmed HA, Awadallah AE, Aboul-Enein AA, Solyman SM, Aboul-Gheit NAK. Catal Lett 2022;152:2789–800.
[91] Sricharoenchaikul V, Atong D. J Anal Appl Pyrolysis 2009;85:155–62.
[92] Fakeeha AH, Ibrahim AA, Khan WU, Seshan K, Al Otaibi RL, Al-Fatesh AS. Arab J Chem 2018;11:405–14.
[93] Awadallah AE, El-Desouki DS, Aboul-Gheit NAK, Ibrahim AH, Aboul-Gheit AK. Int J Hydrogen Energy 2016;41:16890–902.
[94] Ibrahim AA, Fakeeha AH, Al-Fatesh AS, Abasaeed AE, Khan WU. Int J Hydrogen Energy 2015;40:7593–600.
[95] Shilapuram V, Ozalp N, Oschatz M, Borchardt L, Kaskel S, Lachance R. Ind Eng Chem Res 2014;53:1741–53.
[96] Ibrahim AA, Al-Fatesh AS, Khan WU, Soliman MA, Al Otaibi RL, Fakeeha AH. J Chin Chem Soc 2015;62:592–9.
[97] Khan UM, Sarmad Q, Anwar M, Khoja AH, Muhammed Ali SA, Khan ZS, Hassan M, Shakir S. Int J Energy Res 2021;45:20073–88.
[98] Awadallah AE, Mostafa MS, Aboul-Enein AA, Hanafi SA. Fuel 2014;129:68–77.
[99] Shilapuram V, Ozalp N, Oschatz M, Borchardt L, Kaskel S. Carbon N Y 2014;67:377–89.
[100] Ahmed W, Noor El-Din MR, Aboul-Enein AA, Awadallah AE. J Nat Gas Sci Eng 2015;25:359–66.
[101] Fakeeha AH, Barama S, Ibrahim AA, Al-Otaibi R-L, Barama A, Abasaeed AE, Al-Fatesh AS, A. E. A) Sa. Catalysts 2018;8:567.
[102] Awad A, Salam A, Abdullah B. AIP Conf Proc 2017;1891:20030.
[103] Torres D, Pinilla JL, Lázaro MJ, Moliner R, Suelves I. Int J Hydrogen Energy 2014;39:3698–709.

[104] Gunjal PR, Ranade VV. In: Industrial catalytic processes for fine and specialty chemicals. first ed. Elsevier; 2016. p. 263–314.
[105] Guda VK, Steele PH, Penmetsa VK, Li Q. In: Recent advances in thermochemical conversion of biomass. first ed. Elsevier; 2015. p. 177–211.
[106] Amin AM, Croiset E, Constantinou C, Epling W. Int J Hydrogen Energy 2012;37:9038–48.
[107] Zhang J, Li X, Chen H, Qi M, Zhang G, Hu H, Ma X. Int J Hydrogen Energy 2017;42:19755–75.
[108] Abbas HF, Daud WMAW. Int J Hydrogen Energy 2010;35:12268–76.
[109] Pinilla JL, Moliner R, Suelves I, Lázaro MJ, Echegoyen Y, Palacios JM. Int J Hydrogen Energy 2007;32:4821–9.
[110] Qian JX, Enakonda LR, Wang WJ, Gary D, Del-Gallo P, Basset JM, Bin Liu D, Zhou L. Int J Hydrogen Energy 2019;44:31700–11.
[111] Roghair I, Gallucci F, van Sint Annaland M. Adv Chem Eng 2014;45:159–283.
[112] Dhyani V, Bhaskar T. Biomass, biofuels, biochemicals: biofuels: alternative feedstocks and conversion processes for the production of liquid and gaseous biofuels. second ed. Academic Press; 2019. p. 217–44.
[113] Richardson JF, Harker JH, Backhurst JR. Chem Eng Sci 1991;2:1183.
[114] Rajmohan KS, Yadav H, Vaishnavi S, Gopinath M, Varjani S. In: Current developments in biotechnology and bioengineering: resource recovery from wastes. first ed. Elsevier; 2020. p. 459–80.
[115] Ruud Van Ommen J, Nijenhuis J, Coppens M-O. In: The 12th international conference on fluidization - new horizons in fluidization engineering; 2007. p. 184–92.
[116] Grace JR, Bi Xiaotao, Ellis Naoko. Essentials of fluidization technology. first ed. Wiley-VCH; 2019.
[117] Torres D, De Llobet S, Pinilla JL, Lázaro MJ, Suelves I, Moliner R. J Nat Gas Chem 2012;21:367–73.
[118] Hou Z, Gao J, Guo J, Liang D, Lou H, Zheng X. J Catal 2007;250:331–41.
[119] Jung JU, Nam W, Yoon KJ, Han GY. Kor J Chem Eng 2007;24:674–8.
[120] Kunii D, Levenspiel O. In: Fluidization engineering. second ed. Elsevier; 1991. p. 1–13.
[121] Seville J, Wu C-Y. In: Particle technology and engineering. first ed. Elsevier; 2016. p. 67–81.
[122] Yates JG, Lettieri P. In: Fluidized-bed reactors: processes and operating conditions. first ed. Cham: Springer; 2016. p. 1–21.
[123] Seville J, Wu C-Y. In: Particle technology and engineering. first ed. Elsevier; 2016. p. 83–118.
[124] Yates JG, Lettieri P. In: Fluidized-bed reactors: processes and operating conditions. first ed. Cham: Springer; 2016. p. 175–94.
[125] Danafar F, Fakhru'l-Razi A, Salleh MAM, Biak DRA. Chem Eng J 2009;155:37–48.
[126] Allaedini G, Aminayi P, Tasirin SM. Chem Eng Res Des 2016;112:163–74.
[127] Pinilla JL, Suelves I, Lázaro MJ, Moliner R, Palacios JM. Int J Hydrogen Energy 2010;35:9801–9.
[128] Pattipati RR, Wen CY. Ind Eng Chem Process Des Dev 1981;20:705–7.
[129] Bi T, Grace JR, Lim KS. Ind. Eng. Chem. Res 1995;34:4003–8.
[130] Rhodes M. In: Introduction to particle technology. second ed. John Wiley & Sons, Ltd; 2008. p. 169–210.
[131] Geldart D. Powder Technol 1973;7:285–92.
[132] Zhang Y, Ye M, Zhao Y, Gu T, Xiao R, Liu Z. Powder Technol 2015;275:199–210.
[133] Li J, Zhou L, Li P, Zhu Q, Gao J, Gu F, Su F. Chem Eng J 2013;219:183–9.
[134] Lee KK, Han GY, Yoon KJ, Lee BK. Catal Today 2004;93–95:81–6.
[135] Abbas HF, Wan Daud WMA. Int J Hydrogen Energy 2010;35:1160–90.
[136] Keller M, Matsumura A, Sharma A. Chem Eng J 2020;398:125612.
[137] Karimipour S, Pugsley T. Powder Technol 2011;205:1–14.
[138] Ammendola P, Chirone R, Ruoppolo G, Russo G. Chem Eng J 2009;154:287–94.
[139] Parmar KR, Pant KK, Roy S. Energy Convers Manag 2021;232:113893.
[140] Hadian M, Marrevee DPF, Buist KA, Reesink BH, Bos ANR, van Bavel AP, Kuipers JAM. Chem Eng Sci 2022;260:117938.
[141] Dasgupta K, Joshi JB, Banerjee S. Chem Eng J 2011;171:841–69.
[142] Zhou Y, Wang T, Zhu J. Powder Technol 2023;421:118420.
[143] Yasui G, Johanson LN. AIChE J 1958;4:445–52.
[144] Kwauk M. Adv Chem Eng 1991;17:207–360.
[145] Grace JR, Clift R. Can J Chem Eng 1974;52:417–9.
[146] Wen ZQ, Zhang XB, Luo ZH. Chem Eng J 2022;440:135904.
[147] Toei R, Oichi M, Matsuno R, Yamamoto K. J Chem Eng Jpn 1975;7:451–5.
[148] Choi JH, Son JE, Kim SD. Ind Eng Chem Res 1998;37:2559–64.
[149] Kirkpatrick RD, Lockett MJ. Chem Eng Sci 1974;29:2363–73.
[150] Hilligardt K, Werther J. Chem Eng Technol 1987;10:272–80.
[151] Wang T, Xia Z, Chen C. Chem Eng Sci 2019;202:208–21.
[152] Horio M, Nonaka A. AIChE J 1987;33:1865–72.
[153] Darton R, Lanauze R, Davidson J, Harrison D. Trans IChemE 1977;55:274–80.
[154] Knowlton TM. In: Fluidized bed technologies for near-zero emission combustion and gasification. first ed. Elsevier Ltd.; 2013. p. 481–523.
[155] Wen CY, Yu YH. AIChE J 1966;12:610–2.
[156] Ammendola P, Chirone R, Ruoppolo G, Russo G, Solimene R. Int J Hydrogen Energy 2008;33:2679–94.
[157] Chew JW, LaMarche WCQ, Cocco RA. Powder Technol 2022;409:117813.
[158] Ege PE. Investigation of the flow structure in turbulent fluidized beds. Doctoral dissertation. University of Trondheim; 1995. Available at: https://www.osti.gov/etdeweb/biblio/481373. [Accessed 20 October 2023].
[159] Wytrwat T, Yazdanpanah M, Heinrich S. Processes 2020;8:1098.
[160] Bi HT, Ellis N, Abba IA, Grace JR. Chem Eng Sci 2000;55:4789–825.
[161] Zhang Q, Zhao MQ, Huang JQ, Nie JQ, Wei F. Carbon N Y 2010;48:1196–209.
[162] Yun S, Qian W, Cui C, Yu Y, Zheng C, Liu Y, Zhang Q, Wei F. J Energy Chem 2013;22:567–72.
[163] Wang Y, Wei F, Gu G, Yu H. Physica B (Amsterdam, Neth) 2002;323:327–9.
[164] Wei F, Zhang Q, Qian WZ, Yu H, Wang Y, Luo GH, Xu GH, Wang DZ. Powder Technol 2008;183:10–20.
[165] Hao Y, Qunfeng Z, Fei W, Weizhong Q, Guohua L. Carbon N Y 2003;41:2855–63.
[166] Wang Y, Wei F, Luo G, Yu H, Gu A. Chem Phys Lett 2002;364:568–72.
[167] Te Hsieh C, Lin YT, Chen WY, Wei JL. Powder Technol 2009;192:16–22.
[168] Weizhong Q, Tang L, Zhanwen W, Fei W, Zhifei L, Guohua L, Yongdan L. Appl Catal Gen 2004;260:223–8.

https://dspace.org/

Review of the production of turquoise hydrogen from methane catalytic decomposition: Optimising reactors for Sustainable Hydrogen production

Sanyal, Aryamman; Malalasekera, Weeratunge; Bandulasena, Hemaka; Wijayantha, Upul K. G.

2024-06-27
Elsevier
https://doi.org/10.1016/j.ijhydene.2024.05.397
Sanyal A, Malalasekera W, Bandulasena H, Wijayantha KG. (2024) Review of the production of turquoise hydrogen from methane catalytic decomposition: Optimising reactors for Sustainable Hydrogen production. International Journal of Hydrogen Energy, Volume 72, June 2024, pp. 694-715

Downloaded from a DSpace repository. https://dspace.org/